Cluster beam deposition for PV applications

Sjors Geraedts 3036235

6/8/2012

Universiteit Utrecht

Contents

Abstract

Silicon quantum dots are the subject of much research in the photovoltaic sector because of the ability to tune their bandgap. This makes them interesting for applications in a series of solar cell designs. There are many different ways to produce quantum dots, each having its own strengths and weaknesses. In this research, cluster beam deposition is proposed and explored as a way of depositing quantum dots. The installation process of an Oxford Applied Research NC200U nanoclusters source for the deposition of silicon, silver and germanium clusters is described in detail. An extensive characterization of DC deposition of Si clusters has been performed, identifying the influence of aggregation length of the cluster source, argon flow rate and DC magnetron power on the size and density of cluster that are deposited on 1x1 cm silicon wafer substrates.
It has been attempted to produce a silicon quantum dot schottky solar cell, but low deposition yields of the cluster source have so far hampered the progress. A number of possible solutions and suggestions for further research are done.

Acknowledgements

I would like to thank the following people for helping me in my research project:

- Marcel di Vece
- Wilfried van Sark
- Caspar van Bommel
- Ruud Schropp
- Dick van Dam
- Lourens van Dijk
- Diederick Spee
- Catherina Prastani

1. Introduction

In 2008, global electricity production equaled 20.181 TWh[1]. This number is expected to increase to 34.290 TWh by the year 2030, an increase of nearly 70%.[2] 41% of all electricity in 2008 was produced using coal as a fuel, which is the most polluting way of generating electricity currently being used on a large scale. Even though CO_2 emission reductions are agreed upon by most countries, the ratio of coal-produced electricity is expected to rise to 44% by 2030.[2] On the other hand, renewable such as biomass, wind, solar, geothermal, wave and tidal energy are expected to see their share in the electricity mix increase from 2,5% in 2008 to almost 9% in 2030.[2] The need for large-scale application of renewable energy is obvious, but so far, cost considerations have slowed down the implementation of these technologies.

Cost

Solar power is an obvious candidate to be one of the key components of the world's future power supply, as the sun provides twice as much energy to the earth in one year than the total amount of energy that will ever be extracted from all of the Earth's non-renewable resources of oil, gas, coal and uranium combined.[3] The development of photovoltaic (PV) systems took off in the 1960s for space application, and became commercially interesting when prices of PV-modules reached $22 per watt-peak in 1980. Since then, prices have decreased steadily and reached a figure of 3,50-7,70 $\$/W_P$ in 2011.[4] Even at these prices, electricity produced by PV systems is competitive to fossil produced electricity only under very favorable conditions (e.g. in Hawaii), and price reduction continues to be the key to increasing the share of PV in global electricity production.[5] This can be achieved in two ways: (1) increasing the efficiency of PV cells, (2) reducing the production costs.

Both strategies have been applied over the last decades in going from first to third generation solar cells. First generation solar cells were crystalline silicon based, with thick absorber layers using large amounts of silicon. By developing thin-film techniques, second generation solar cells require much smaller amounts of silicon and therefore production costs decrease. For the third generation, research is focused on improving the efficiencies of thin-film devices by introducing multiple energy levels to ultimately yield a high efficiency, low cost PV cell which produces electricity at similar or lower prices than coal-fired power plants.

Efficiency

The well-known Shockley-Quiesser limit states that the maximum efficiency a single-bandgap device can achieve for unconcentrated light is 31%.[6] About half of the power loss is due to two mechanisms: The inability to absorb photons with energy lower than the bandgap, and thermalization losses of photons with energy exceeding the bandgap. A device design which utilizes multiple energy levels can harvest a larger part of the solar spectrum and thereby circumvent the

Shockley-Queisser limit.[7] Three different approaches have been suggested for applying multiple energy levels: (1) increasing the number of energy levels; (2) Multiple carrier generation per high energy photon, or single carrier generation from multiple low energy photons; (3) Capturing carriers prior to thermalization. Tandem cells use strategy 1 by stacking solar cells with different bandgaps on top of each other, with the highest bandgap cell intercepting the sunlight first. Multiple Exciton Generation (MEG) cells and hot carrier cells are examples of strategies 2 and 3 respectively, and will be further explained below.[7]

Quantum dots

First discovered in 1981 by Ekimov[8], quantum dots (QDs) are portions of matter whose excitons are confined in 3 dimensions. An exciton is quasiparticle formed by an electron and a hole that are attracted to each other by the electrostatic Coulomb force, and which can be formed when a semiconductor absorbs a photon. This confinement effect implies for semiconductors that the electronic properties of the quantum dot are related to its dimensions. In this way it's possible to tune the effective bandgap of the semiconductor by controlling its size: Decreasing the dimensions of the QD to values below a certain value leads to quantization of allowed energy states. This critical value is known as the exciton Bohr radius of the quantum dot and its definition is given in equation 1.

$$a_b^* = \varepsilon_r \left(\frac{m}{\mu}\right) a_b$$ **Equation 1**[9]

In which a^*_b is the exciton Bohr radius, ε_r is the dielectric constant, m the mass of the QD, μ the reduced mass and a_b the standard Bohr radius (=0.053 nm).

The increase in energy for the n'th confined energy level is given by:

$$\Delta E_n = \frac{\pi^2 \hbar^2}{m^* a^2}\left(n_1^2 + n_2^2 + n_3^2\right) \quad = \quad 3\frac{\pi^2 \hbar^2}{m^* a^2}.n^2 \quad \text{for } n_1 = n_2 = n_3$$ **Equation 2** [9]

Where ħ=h/2π is the reduced Planck's constant, m* is effective mass of the particle, *a* is the width of the QD and n_1 n_2 and n_3 are the quantum numbers in each confined dimension.[9]

As the QD size decreases, ΔE_n increases, thereby increasing the effective bandgap. For a spherical Si QD with infinite confining barrier potential, the first quantized ground state E_1 is given by:

$$E_1 \approx E_g + \frac{609}{\left(\sqrt{3}/2\right)^2 \cdot a^2}$$ **Equation 3** [9]

a is in Angstroms and E_1 and E_g(the bulk bandgap of Si) are in eV.[9]

An additional effect is that the localization of electrons and holes in a QD leads to reflection or folding of phonons in k-space. This means that the conservation of momentum requirement is

relaxed. While bulk indirect semiconductors (like silicon) can only absorb a photon and create an exciton if a phonon is absorbed simultaneously (decreasing the probability), a quasi-direct bandgap is created for a Si QD, relaxing this requirement.[9] The ability to tune the effective bandgap of a semiconductor by controlling QD size, and the creation of a quasi-direct bandgap attracted the attention of solar cell research, in which QDs are applied in several 3rd generation solar cell designs trying to harvest a larger part of solar radiation by using one of the three abovementioned strategies. Apart from Si, several other QD materials have been developed, of which CdSe and PbS are two of the most widely used, especially for Multiple Exciton Generation (see sectie 2.1.3). However, CdSe is a toxic material and thus not suitable for widespread use.[10] PbS is promising because of its low bandgap (0,41 eV), large exciton Bohr radius (18 nm) and strong quantum-size effect.[11]

2. Theory

2.1 QD solar cell designs

2.1.1 All Si tandem cell

A classic tandem cell consists of subcells of different semiconductor materials of increasing bandgap, placed on top of eachother in such a way that the highest bandgap cell intercepts the sunlight first.[7] To achieve the highest efficiency, the subcells must be optimized by choosing the appropriate bandgap, thickness, junction depth and doping characteristics. The highest efficiency tandem devices are made using single-crystal III-V materials, such as InGaP and InGaAs, which are grown using expensive epitaxial techniques.[7] In a 2-cell tandem stack with a crystalline silicon bottom cell (bandgap = 1.1 eV), the optimal bandgap for the top cell is 1.7 eV. By using Si QDs of a suitable dimension, a silicon top cell can be produced having this optimal bandgap. In this way, an all Si tandem cell is created which avoids the use of expensive and rare III-V materials.[7, 12]

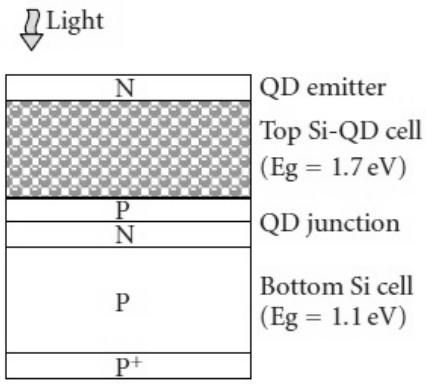

Figure 1 Two-cell tandem solar cell with a Si bottom cell [12]

2.1.2 Intermediate band solar cell (IBSC)

This device design introduces an additional energy level in the forbidden bandgap of a conventional semiconductor, thereby creating the possibility of a two-step transition from the valence band to the conduction band. This allows two photons with sub-bandgap energy to create an electron-hole pair, whilst keeping the regular valence band-conduction band transition in place.[13] If the sub-bandgap absorbers form a continuous band of levels (isolated from the valence and conduction band), the delocalization of carriers means that the two photons not necessarily have to be absorbed by the same electron. This gives a longer lifetime to the intermediate level, which increases the chance of absorption of second photon. To optimize this effect, the intermediate band should be half-filled with electrons and thus have a Fermi-level at half the band energy.[7] Figure 2 shows the band diagram of such a cell. As can be seen, the intermediate band's Fermi energy lines up with the cells Fermi level and the intermediate band is half filled with electrons. Photons with energy J_l can excite electrons from the valence band to the intermediate level, and photons with energy J_h can excite electrons from the intermediate level to the conduction band. Direct excitation from the valence band to the conduction band is also still possible for photons with high enough energy. QDs have been proposed for the intermediate band, as they provide a true 0-density of states between the confined states and the conduction band. This is expected to prevent quick relaxation of electrons from the conduction band to the confined state by means of the phonon-bottleneck effect.[13] This effect states that longitudinal optical (LO) phonon emission is forbidden in QDs because of the discrete nature of the energy levels, unless the level separation ΔE equals the LO phonon energy. Because of this, carriers are unable to relax to ground levels and remain at excited levels.[14]

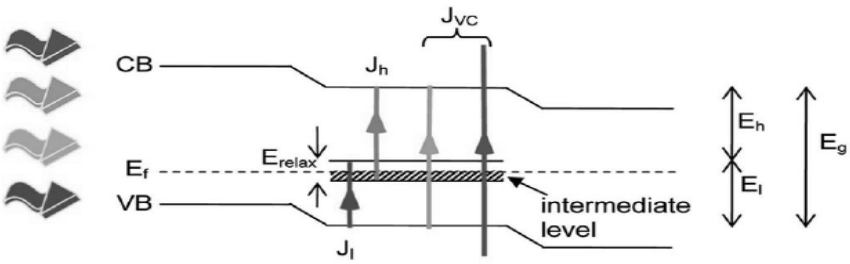

Figure 2 Intermediate band solar cell. Sub-bandgap photons are absorbed by the transitions to and from the intermediate level (E_h and E_l) [11]

2.1.3 Multiple exciton generation (MEG)

Where previous two designs used strategy 1 (increasing the number of energy levels), the MEG cell is an example of strategy 2: Multiple carrier generation per high energy photon.[7] A photon with an energy exceeding the bandgap of a semiconductor will produce an electron with excess energy (having energy higher than the band minimum), which is called a 'hot' electron. In conventional solar cells these hot electrons lose their excess energy by thermalization through

successive phonon emissions. MEG cells try to put this energy to good use by a mechanism called impact ionization, which states that under favorable conditions the excess energy of a hot electron can be transferred to excite a second electron and in this way create a second electron-hole pair.[7, 15, 16] For this to work, the minimum energy of the absorbed photon has to be ≥ $2E_g$. QDs are very suitable for this strategy because of enhanced Coulomb interaction and relaxation of momentum conservation, which greatly improves the rate of impact ionization when compared to bulk material.[7, 16]

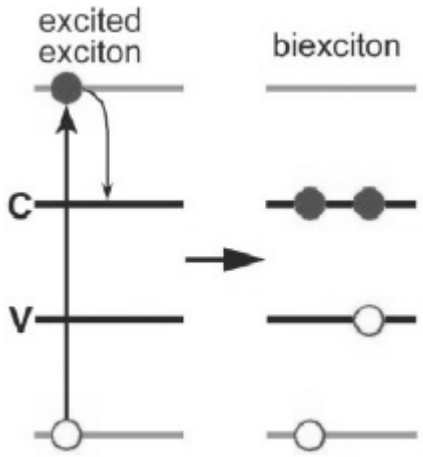

Figure 3 Multiple exciton generation: 1 high energy photon produces multiple electron-hole pairs [16]

2.1.4 Hot carrier cell

The third strategy to increase efficiency in third generation solar cells is applied in hot carrier cells. As one would expect, this device design aims to extract hot carriers before they lose their excess energy through thermalization.[7] To achieve this, the rate of carrier cooling needs to be slowed down from the picoseconds to the nanoseconds timescale, so that extraction can take place.[17] The phonon bottleneck effect has been suggested as a means to slow cooling and modifying the phononic band structure of QD superlattices is a way to achieve this, but much research is left to be done.[17] A second requirement for hot carrier cells is the extraction of carriers through contacts that allow only a very narrow range of energies. This is necessary to prevent cold carriers from entering the contact, which in turn could cool the hot carriers en thereby increase the entropy. [7, 17]

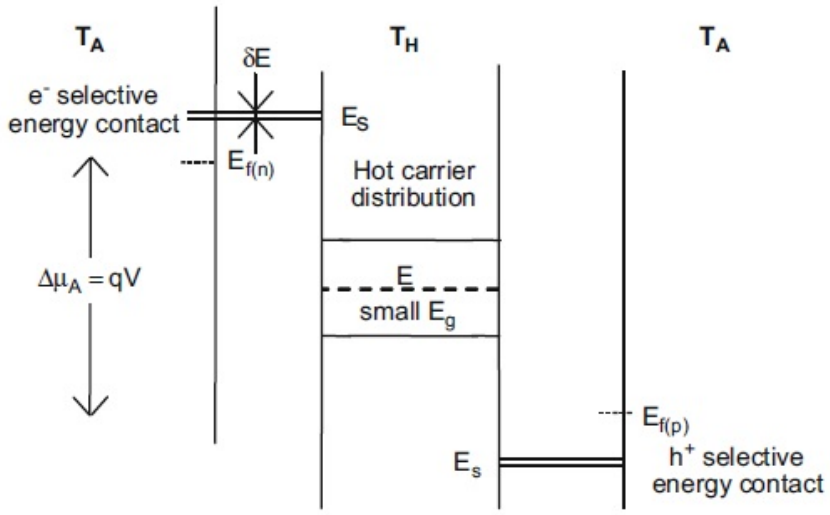

Figure 4 Band diagram of a hot carrier cell with selective contacts [17]

Device design	Efficiency limit
Single junction µC-Si	29%[12]
2-cell all Si-tandem	42.5%[12]
3-cell all Si- tandem	47.5%[12]
IBSC	48%[7]
MEG cell	42%[7]
Hot carrier cell	65%[17]

Table 1 Overview of theoretical efficiency limits of different solar cell designs

2.2 Si QD production

Silicon QDs can be produced using different approaches, each having its own specific characteristics like deposition method, deposition speed, temperature and QD size control. A few of these approaches will be discussed briefly before going into more detail for the Cluster Beam Deposition (CBD) technique used for this project.

2.2.1 Multilayer superlattice approach

Based on the superlattice approach to produce silicon QDs[18], the multilayer superlattice approach uses RF magnetron sputtering to deposit alternating layers of SiO_2 and SRO (silicon rich oxide, formed by co-sputtering of Si and SiO_2) of thicknesses down to 2 nm.[9] Deposition of multiple layers, typically consisting of 20 to 50 bi-layers, is followed by an anneal in N_2 from 1050 to 1150°C. During the annealing process, the excess silicon in the SRO layer precipitates to form Si QDs between the stoichiometric SiO_2 layers.[9] For Si QDs in SiO_2 the precipitation occurs according to the following:

$SiO_x \rightarrow \frac{x}{2} SiO_2 + (1-\frac{x}{2})\ Si$ [9, 18]

In a similar fashion, silicon QDs have been produced in other dielectric matrices such as Si_3N_4 and SiC.[9] By controlling the stoichiometry of the SRO, the size of the produced QDs can be controlled: the average Si QD diameter increases from 2,5 nm to 4 nm as the O/Si ratio decreases from 1,30 to 0,86 (figure 5).[9]

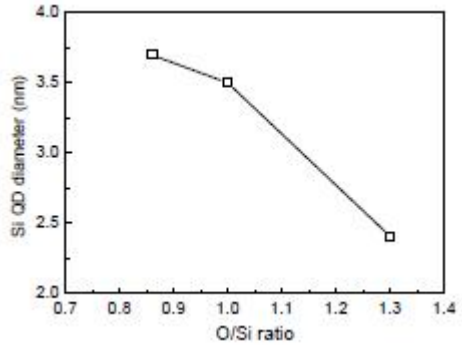

Figure 5 QD diameter as a function of O/Si ratio in annealed SiOx/SiO2 multilayer films [9]

2.2.2 PECVD

Silicon QDs have been grown by Plasma Enhanced Chemical Vapour Deposition (PECVD) at 300°C without any post-annealing, using silane and nitrogen as reactant gas sources.[19, 20] Varying the N_2 flow rate is a way to control the dot size. It's been suggested that the increase in the N_2 flow rate promotes the formation of Si dangling bonds acting as nucleation sites.[19] Increasing the N_2 flow rate results in more closely packed but smaller silicon QDs, since the silane flow rate is kept constant.[19] Adding NH_3 to the gas mix intensifies photoluminescence, which has been attributed to more efficient passivation of nonradiative defects at the dot-matrix interface, thanks to the extra hydrogen (of NH_3) available during the growth process.[20]

2.2.3 Colloidal QDs

Colloidal QDs primary advantage is they're low costs because are processed in solution. Therefore, solar cells made up of colloidal QDs can be spin-coated, spray-coated or inkjet printed onto their substrates without a high temperature step, making them suitable for cheap, flexible, plastic substrates. These production techniques are also easily upscalable, which reduces production costs even more.[21] A Schottky junction solar cell was produced from colloidal silicon QDs by Liu and Kortshagen.[22] Silicon QDs were synthesized through a non-thermal plasma reactor and collected downstream on stainless steel meshes, after which they were dispersed in 1,2-dichlorobenzene. The QDs were then spin-coated onto a indium tin oxide coated glass substrate to form a 250 nm thin film. Finally, a 100 nm aluminum layer was deposited on top as the electrode.[22] The device clearly showed a photovoltaic effect, although the efficiency was only 0.02%, with a fill factor of 0.26.[22]

2.3 Schottky QD Solar Cell

2.3.1 Band diagram & I-V characteristics

Schottky solar cells are among the simplest photovoltaic devices that can be fabricated. It consists of a metal and a semiconductor forming a rectifying junction. The difference in workfunction between the metal and the semiconductor causes band bending in the semiconductor. The resulting depletion region causes a built-in electric field which causes separation and transportation of photogenerated electron-hole pairs. Figure 10 shows the band diagram of a Schottky solar cell consisting of aluminum on a PbS QD film.[23] For this particular cell, an efficiency of 1.8% was achieved under simulated solar illumination (100 mW cm^{-2}), with V_{oc}=0.33 V and J_{sc}=12.3 mA cm^{-2}.[23]

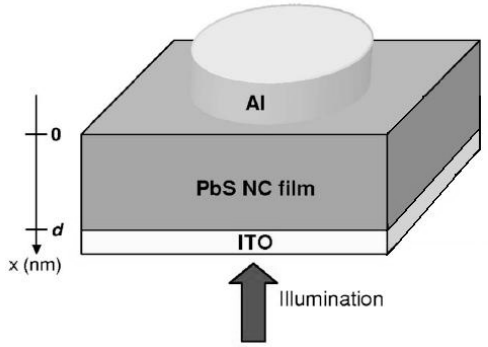

Figure 6 Schematic view of PbS NC Schottky solar cell[23]

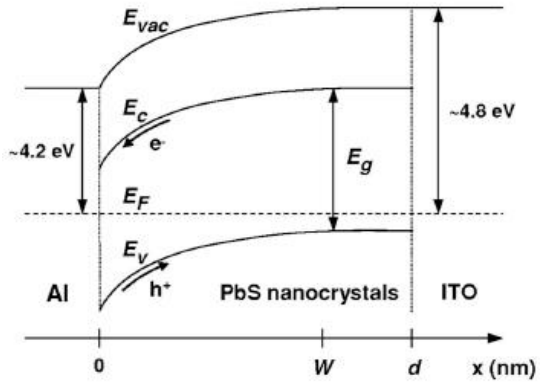

Figure 7 Band diagram of PbS NC Schottky solar cell [23]

A Schottky junction solar cell based on silicon QDs has been reported by Liu and Kortshagen.[22] The colloidal silicon QDs were spin-coated onto an ITO layer, an aluminum contact was then deposited on top (figure 12). The size of the QDs was in a range of 10-20 nm, which is much larger than the exciton Bohr radius for silicon which is ~5 nm. A comparison of the I-V characteristics under AM1.5 and dark conditions clearly show a photovoltaic effect. An efficiency of 0.02% was achieved under AM1.5, with a V_{oc}=0.51 V and J_{sc}=0.148 mA cm^{-2} (figure 13).[22] Although this proves the working

principle of this type of cell, the achieved efficiency leaves much room for improvement and further research.

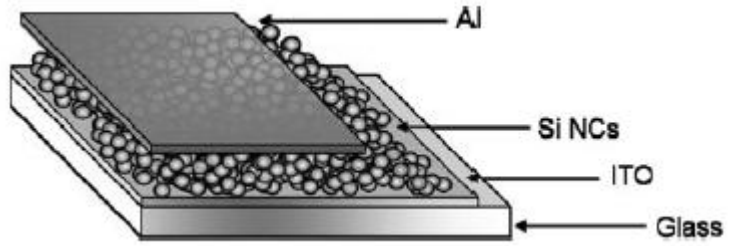

Figure 8 Si QD Schottky solar cell [22]

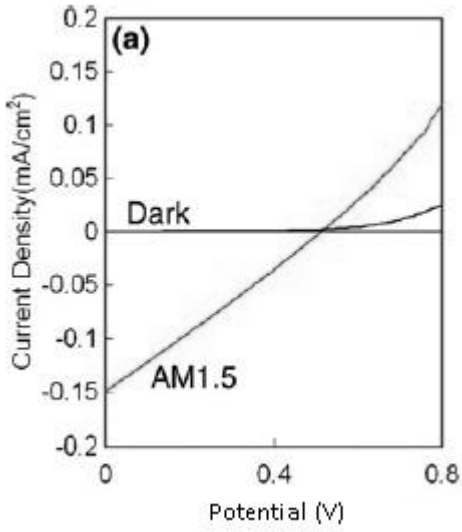

Figure 9 J-V characteristics of Si QD Schottky solar cell[22]

There are a number of possible reasons for this very low efficiency: (1) The almost linear I-V characteristic in the fourth quadrant suggests that electron-hole recombination is a significant loss-channel in this device.[22] (2) Strong absorption is only seen in the blue and ultraviolet range of the spectrum. This is because the QDs still behave as an indirect semiconductor. They are not small enough to create a quasi-direct bandgap.[22] (3) Agglomeration of QDs caused a rough morphology of the QD layer. Agglomerates of up to 1 µm were observed, which is very large when compared to the 250 nm QD layer. (4) The QDs were not doped. Doping has proven to dramatically decrease resistivity in silicon QDs by providing extra charge carriers, similar to doping of bulk semiconductors.[24,25]

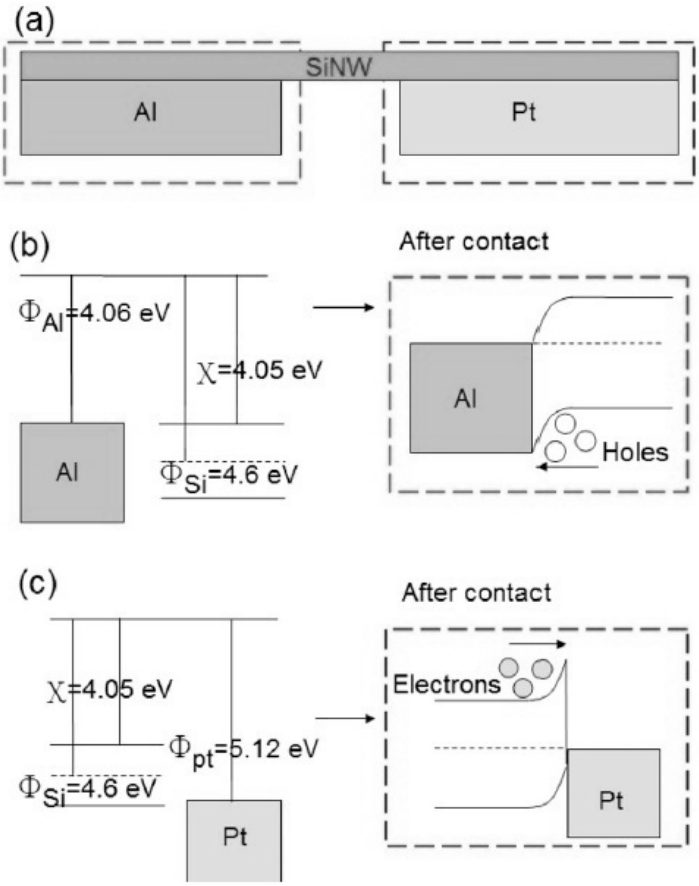

Figure 10 Band diagrams of SiNW Schottky solar cell before and after contact is made [26]

Figure 10 shows the band diagram of an undoped silicon nanowire Schottky solar cell, both before and after contact is made.[26] Figure b shows the low work function aluminum contact before and after contact is made. Before contact, the Si Fermi level is deeper than the top of the Al band. After contact, electrons flow from the aluminum into the silicon raising the Fermi level of the silicon and causing band bending. Figure c shows what happens at the high work function contact: The Fermi level is higher than the top of the Pt band, so after contact electrons flow into the Pt, causing the silicon Fermi level to drop and thereby causing band bending. The built in electric field which is created in this way on both contacts is the driving force of the charge separation that takes place. Both holes and electrons need to overcome a barrier to be collected in the contacts. The barrier heights are determined by the differences in work function between the contacts and the semiconductor.

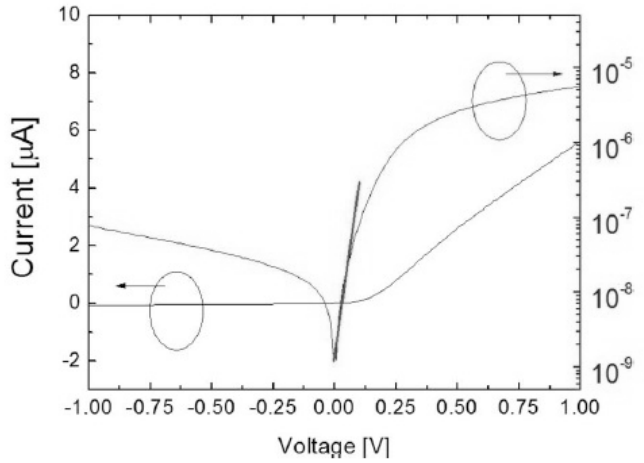

Figure 11 I-V characteristics of SiNW Schottky solar cell [26]

Figure 11 shows the dark I-V curve of the nanowire schottky solar cell.[26] The I-V characteristics can be described by the thermionic emission theory equations:

$$J = J_s(e^{qv/nkT} - 1)$$ **Equation 4** [26]

$$J_s = A^{**}T^2 \exp\left(-\frac{q\phi_B}{kT}\right)$$ **Equation 5** [26]

Where J_s, kT, A** and ϕ_B are saturation current density, thermal energy (eV), Richardson constant and barrier height respectively. The current density thus depends on bias, temperature and the maximum saturation current density. The saturation density depends on temperature and the barrier height seen by electrons and holes that want to enter the contact. Lowering the barrier height increases the saturation current density. When surface states are neglected, a general expression of the barrier height can be simplified to be:

$$\phi_B = \frac{-kT}{q}\ln\left(\frac{J}{e^{qv/kT}}\frac{1}{A^{**}T^2}\right) = \frac{kT}{q}\ln\left(\frac{A^{**}T^2}{J_s}\right)$$ **Equation 6** [26]

2.3.2 Light absorption

As described earlier, the small dimensions of quantum dots (QDs) gives them unique optical and electronic properties when compared to bulk material. Decreasing the dimensions of a QD below the materials Bohr-radius causes quantization of allowed energy states. As a result, the light absorption characteristics also depend on the QD size. Photoluminescence (PL) measurements of silicon quantum dots embedded in a Si-rich SiN matrix show that the PL emission peak energy exhibits a blueshift for smaller size QDs.[27,28] (Figure 12)

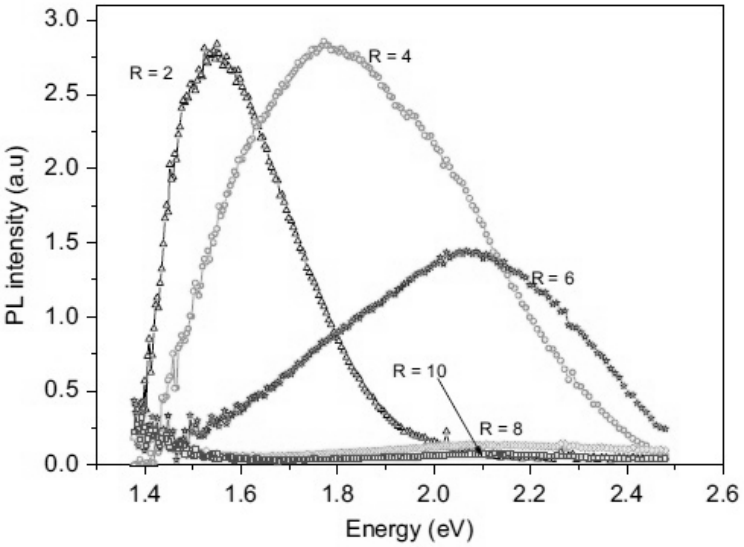

Figure 12 PL measurements of Si QDs in a SiN matrix. QD size decreases for increasing R [28]

The shift in the PL peak is caused by bandgap expansion due to quantum confinement. The relation between QD size and bandgap expansion was first calculated for silicon QDs by Wang and Zunger in 1994.[29] They concluded that a band gap vs size curve exists for a few prototype QD shapes, and that the band gap is rather insensitive to orientation and shape as long as the shape is not too prolate.[29] They're theoretical model has been confirmed with experimental data, as can be seen in Figure 13.

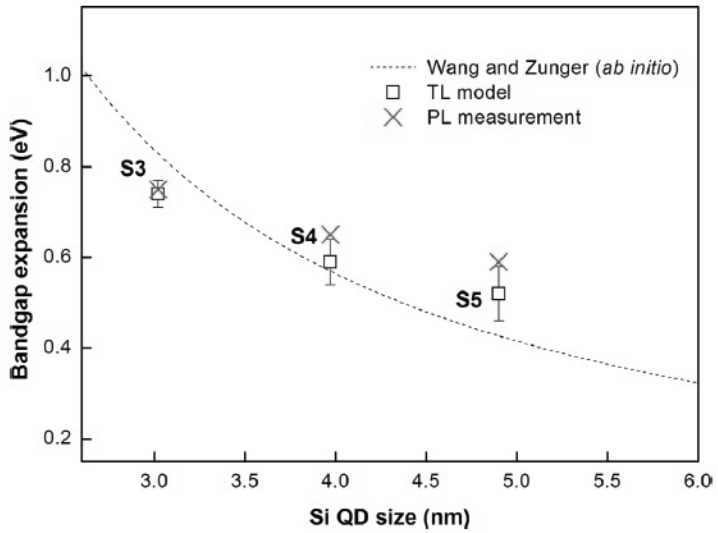

Figure 13 Band gap expansion of Si QD vs QD size [30]

2.3.3 Carrier Transport

Mobility of charge carriers in the absorbing material is essential for solar cells. If mobility is limited, recombination of electrons and holes will take place before they can reach the electrodes, and little or no power can be extracted. Since QDs can be seen as isolated particles, the transportation method of charge carriers between them is through resonant tunneling or hopping. A number of factors influence the ease with which tunneling can take place, en thereby have major impact on the efficiency of carrier transport in a QD network.

The effect of the QD size and the inter-dot distance on the mobility has been researched by calculating the Bloch mobility for various values of the two.[31] The Bloch mobility is the mobility of a particle placed in a periodic potential (in this case a superlattice) and is calculated with equation 7.

$$\mu = \frac{e\tau}{m^*_{\mathrm{QDS}}}$$ **Equation 7**[31]

Where e, τ and m* are the electron charge, carrier scattering time and electron effective mass, respectively.

Figure 14 a) Bloch mobility vs dot size (inter-dot distance 1 nm) b) Bloch mobility vs inter-dot distance (QD size 2x2x2 nm) [31]

Figure 14 shows plots of the QD size and the inter-dot distance vs the calculated Bloch mobility. From these plots, it is clear that the inter-dot distance has a much larger impact on the mobility than the QD size: whereas the mobility only decreases slightly for increasing dot size, it decreases by several orders of magnitude for increasing inter-dot distance.

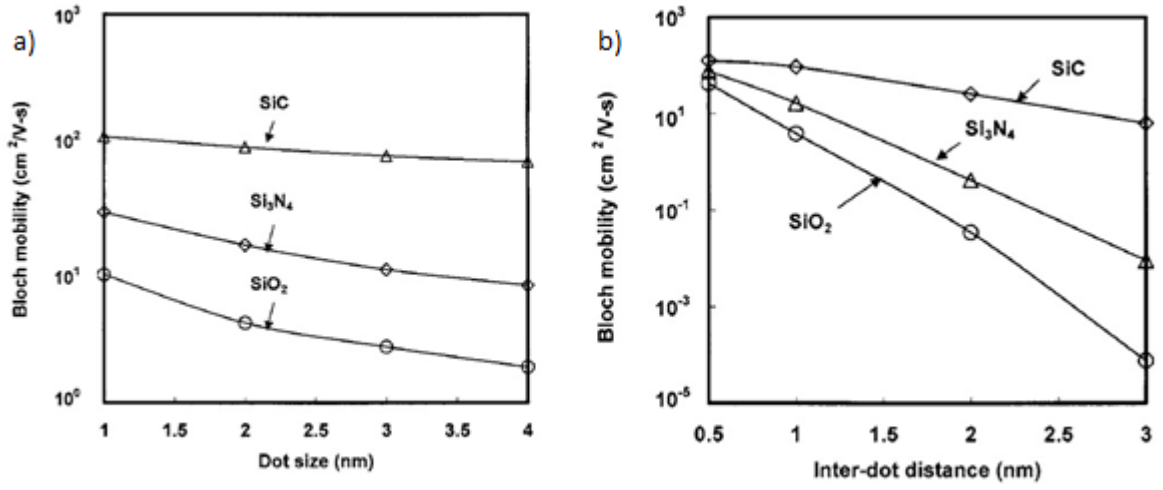

Figure 14 a) Bloch mobility vs dot size (inter-dot distance 1 nm) b) Bloch mobility vs inter-dot distance (QD size 2x2x2 nm) [31]

Another factor influences the mobility of carriers is the barrier between adjacent QDs. This barrier can be a dielectric matrix in which the QDs are embedded, like SiO_2, Si_3N_4 or SiC.[9] The barrier height

depends on the matrix, and tunneling probability is dependent on this barrier height through equation 7:

$$T_e \approx 16 \exp\left\{-d\sqrt{\frac{8m^*}{\hbar^2}\Delta E}\right\}$$

Equation 8[9]

In which T_e is the tunneling probability, d is the barrier width (= the spacing between QDs), m* is the effective electron mass, $\hbar$ is Planck constant/2π and ΔE is the difference between the CB edge of the matrix and the confined energy level of the QDs. The tunneling probability between quantum dots thus depends on barrier height and barrier thickness: closer spaced QDs increase the probability, as does a lower matrix barrier height.[9] Figure 15 show the band alignments of silicon and its carbide, nitride and oxide, all three of which can be applied as matrix for silicon QDs. Silicon carbide has the lowest barrier, followed by the nitride and the oxide. This explains why Bloch mobilities are highest for SiC matrix in Figure 14. A uniform size distribution is important to prevent trapping of electrons in QDs: for quantum dots, difference in size means difference in energy levels. If a QD of a certain size is surrounded by QDs of different sizes, an electron might not be able to tunnel to an adjourning QD since there's no suitable energy level available. In this way, an electron can get trapped in a QD and not take part in the conduction process.

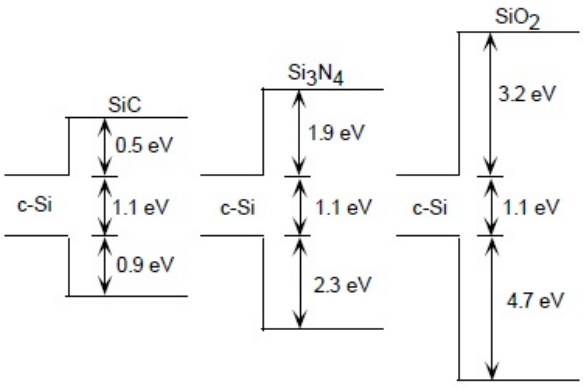

Figure 15 Bulk band alignments between silicon and its carbide, nitride and oxide [9]

Figure 16 shows the band diagram for a QD between two barriers, a simplified model of a QD solar cell. At zero applied voltage (V_a=0), the metal Fermi level is below the first ground level of the QD, and no tunneling can occur. As V_a increases to values at or above the confined energy levels of the QD, electrons can resonantly tunnel through the barriers, causing current I_1 and I_2, seen in figure b.[32]

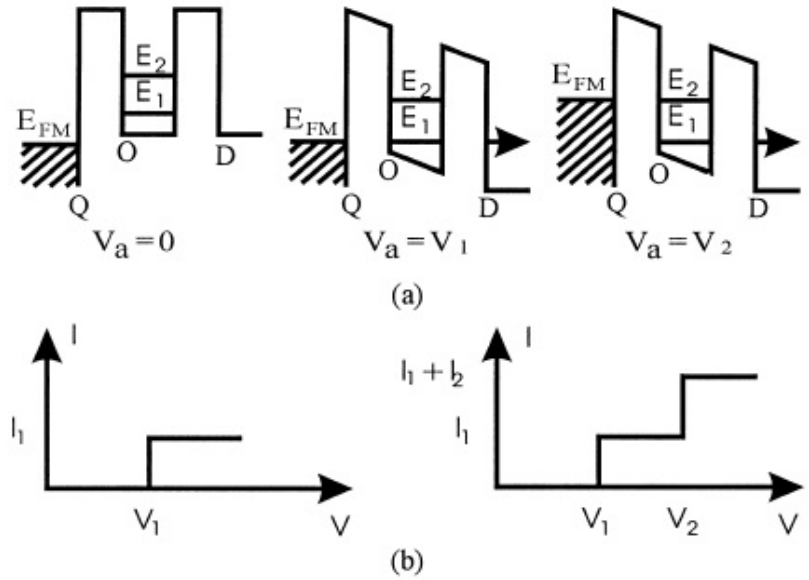

Figure 16 Charge transport resonant tunneling between QDs[32]

2.3.4 Doping

Improving the conductivity of QD devices through impurity doping of the QDs has proven to be a challenge. The introduction of a few impurity atoms into a structure containing only a couple hundred up to a couple thousand atoms may lead to their expulsion to the surface or may compromise the crystal structure of the QD.[33] Adding a single impurity atom to a QD with a diameter of 4 nm (containing 1000 atoms), results in a doping level of $7x10^{19}$ cm^{-3}, well within the heavily doped regime for bulk semiconductors.[33] A first problem that faces the doping of QDs is that the impurity solubility is much lower than in the bulk, and therefore the impurities are expelled because of thermodynamics.[34] Secondly, QDs with an extra electron or hole can act as a strong reducing or oxidizing agent, respectively, and electrochemical reactions at the surface can consume the carrier, although this only occurs when QDs are in solution surrounded by reactive gases.[34]

There are several strategies to overcome the challenges and doping of quantum dots has been shown to be effective as a ways to improve electrical conductivity. One of those strategies and the results on the conductivity of silicon QDs will be discussed in more detail below.

N-type doping of the QDs has been achieved by co- sputtering of Si, SiO_2 and P_2O_5, whilst keeping to the same procedure as the multilayer approach mentioned above.[24, 35] The dark resistivity of the doped samples containing 0,1 at% P is seven orders of magnitude lower than that of the undoped samples. At 0,35 at% P, the resistivity is only five orders of magnitude lower than that of the undoped samples, which may result from the saturation of P in the Si QDs and thus aggregation

of P around the Si QD/SiO_2 interface.[24] As the P concentration increases from 0% to 0.1 at%, the activation energy E_a (calculated from the relation R(ohm)=exp(E_a/kT)) decreases from 0.527 to 0.101 eV. This decrease in E_a indicates that the Fermi energy moves towards the conduction band, suggesting effective n-type doping of the Si QDs.[24]

P-type doping of the QDs has been achieved by co-sputtering of Si, SiO_2 and B, whilst keeping to the same procedure as the multilayer approach mentioned above. The B concentration was controlled by varying the power supplied to the boron target (P_B=0 W, 10 W or 30 W).[25] The dark resistivity decreases 6 orders of magnitude from the undoped sample to the sample with P_B=30 W (from 10^8 Ω to 10^2 Ω), and the activation energy E_a decreases from 0.527 eV to 0.099 eV.[25] The combination of these findings indicates that the Fermi energy moves towards the valence band, suggesting effective p-type doping of the Si QDs.[25]

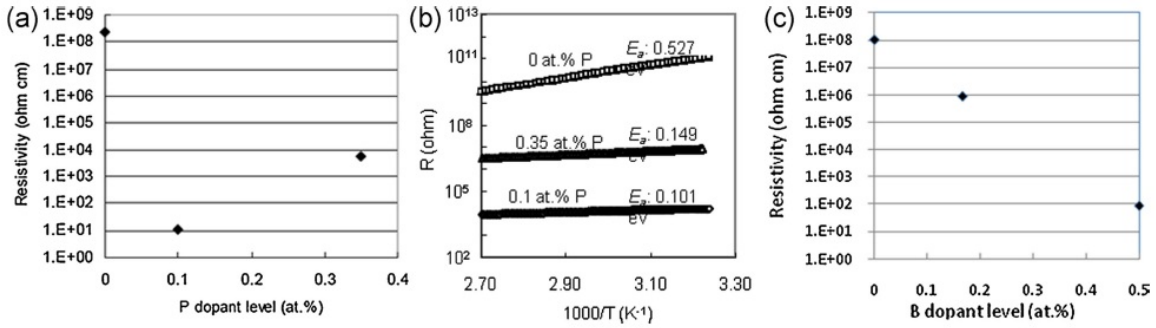

Figure 17 a) effect of P dopant level on resistivity of Si QDs b)Temperature dependence of resistivity c) effect of B dopant levels on resistivity of Si QDs[36]

3. Cluster source installation and characterization

3.1 Theory

In section 3.1 theory about clusters, magnetron sputtering, cluster beam formation and cluster deposition will be discussed. All of which are essential to understanding the working mechanism of the cluster source.

3.1.1 Clusters

Atomic clusters are aggregates of atoms which can be formed from one chemical element or from two or more different elements. Their size varies from a few up to a few thousand atoms, forming a transition between individual atoms (or molecules) and bulk material.[37]. Depending on size and composition, clusters exhibit different binding types as well as different geometric and electronic structures.[37] Research to determine the atomic structure of silicon clusters (Si_n) has been driven by continuous miniaturization of electronic devices and by the discovery that nanoscale material exhibits different behavior than bulk material. Small silicon clusters (n <15) are highly

reactive because of a relatively large amount of dangling bonds[38]: In bulk material, silicon is bonded to four other Si atoms, but at the interface there are unsatisfied (dangling) bonds. As the cluster size decreases, the surface/ volume ratio increases and so will the relative abundance of dangling bonds.[39] These dangling bonds establish localized defect states within the forbidden bandgap of the silicon cluster, which can act as non-radiative recombination centers.[39] Hydrogenation of the cluster or introduction of a metal atom in the cluster dramatically increases the stability by passivation of these dangling bonds.[38, 40] This decreases the number of defect states which decreases the non-radiative recombination and thereby improves the material quality.[39]

3.1.2 Magnetron sputtering

Magnetron sputtering is a magnetically enhanced form of diode sputtering which emerged in the 1970s. It's a high-rate vacuum technique for depositing metals, alloys and compounds onto a wide arrange of materials and offers several advantages over other vacuum coating techniques: (1) high deposition rate, (2) ease of sputtering any metal, alloy or compound, (3) high-purity films, (4) extremely high cohesion of films, (5) excellent coverage of steps and small features, (6) ability to coat heat-sensitive substrates, (7) ease of automation, (8) excellent uniformity on large-area substrates.[41] Figure 18 shows a schematic diagram of a magnetron sputtering source. Electrons are emitted from the cathode and accelerated towards the positive electrode. When the electrons have sufficient energy they can ionize gas atoms (for instance argon), forming positive gas ions (a plasma). These positive ions then move towards the cathode and impinge on its surface, where the impact creates secondary electrons and sputters atoms (or particles) from the surface.[41] The magnetron uses the principle of applying a specially shaped magnetic field to the sputtering target, thereby trapping primary and secondary electrons in a localized region close to the cathode and greatly increasing the chance of experiencing an ionizing collision with a gas atom. This greater ionization efficiency leads to an increased ion current density onto the target and thus to an increase in the sputtering rate.[41]

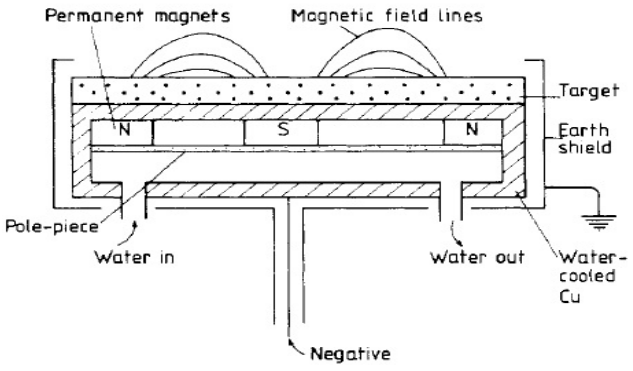

Figure 18 Schematic diagram of a magnetron source

Since the electrons and thus the plasma is localized and concentrated at a specific region in front of the target, the erosion of the target is also highest in this region and a characteristic erosion groove is formed on the target (Figure 19).[41]

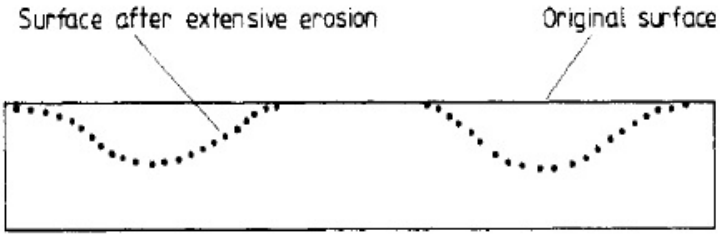

Figure 19 Typical erosion profile of a magnetron target[41]

The two types of magnetron sputtering most commonly used are direct current (DC) and radio frequency (RF). In the DC mode the target is directly conducting electricity. This is the simplest and cheapest of magnetron processes and can produce deposition rates of several micrometers per minute, but is obviously only suitable for conducting targets.[41] RF sputtering was developed to enable sputtering of dielectric materials. When RF power is applied to a target it must be capacitively coupled such that a DC sheath potential is able de develop on the surface of the target. At the high frequency typically used for RF sputtering ions and electrons have different mobilities in the fluctuating field, which means they move different distances during each half cycle. An excess electron current is the result of this difference in mobility. Since the system is capacitively coupled, no net charge can be transferred which results in a negatively biased electrode to compensate for the excess electron current. In this way a DC negative voltage is produced on the cathode surface. Because this DC voltage is present, surface ion bombardment occurs similar to DC magnetron sputtering and so it is possible to sputter insulating materials in this way. Metallic materials can also be sputtered by RF sputtering.[41] The sputtering yield (defined as the number of atoms ejected from a target surface per incident ion) and the deposition rate are usually much lower for RF sputtering when compared to DC.[41]

Because of too low sputtering yields in the experimental part of the research, a literature study was done to get a better understanding of the parameters used during Si and Ge sputtering and use this information to achieve higher sputtering yields. Table 2 is an overview of DC and RF sputtering conditions for silicon and germanium targets. It can be seen that the highest sputtering yields are achieved with high power (kW range) and/or high Ar flow rates (>100 sccm).

Target type(Radius)	Base P(mbar)	Working P(mbar)	Target-substrate distance(cm)	Sputtering type	Power	Deposition rate (nm/min)	Ar flow rate (sccm)
c-Si (5 cm)[42]	2.00E-06	2.00E-03	7	Pulsed DC (100 kHz)	360-1200 mW/cm2		
a-Si[43]		1.30E-02		DC	2250 mW/cm2		
B-doped Si[44]	< 1.33E-7	1.07E-02		DC	1.5 kW	23	
B-doped Si[4445]	< 1.33E-7	1.87E-02		DC	1.5 kW	19	
B-doped Si[44]	< 1.33E-7	1.07E-02		DC	2.5 kW	37	
B-doped Si[44]	< 1.33E-7	1.87E-02		DC	2.5 kW	30	
Si[45]		1.00E-03		Pulsed DC	100 W		
B-doped Si[46]	1.50E-08	5.00E-03	9	Pulsed DC (150 kHz)	50 W 200V	3	250
Si (5 cm)[47]	1.00E-05	1.00E-03	10	DC			
Si[48]	2.55E-05	9.3E-02 - 4.4E-01	2-5	DC			
a-Si[49]	< 4E-05			DC	100 W (2.2W/cm2)	12.0-72	
Si (7.5 cm)[50]				DC	600 W	20.4-24	
Si [51]	1.00E-05	3.70E-02	8.5	DC	275 W	67	
Si[51]	1.00E-05	3.70E-02	8.5	RF	225-675	1.67	
Si (5 cm) [52]		4.03E-03 - 3.26E-02	7	RF	100 W	.18-.48	10
Si[53]	3.00E-06		7	RF	100-800 W	0.6-24	7
Si[54]		1.20E-01			50-150 W		
Ge[55]	1.00E-05	4.00E-02	4	DC	110 W		
Ge[56]	1.07E-08	2.20E-06	10	Pulsed DC (350kHz)	550 W	13	250
Ge[57]	1.07E-08	2.20E-06	10	Pulsed DC (350kHz)	800 W	17	200

Table 2 Sputtering conditions of Si and Ge targets

3.1.3 Cluster beams

Cluster beam deposition (CBD) is a technique in which a beam containing conglomerates of atoms is used to deposit nanoparticles on suitable substrates or into matrices.[58] The technique was first mentioned in the 1950's and has been developed and refined ever since.[37] There is a range of techniques for cluster production, each having its own advantages and disadvantages. For this research a gas condensation nanocluster source is used, in which the material is sputtered (DC or RF magnetron) into a cooled (water or nitrogen), high pressure aggregation/drift region. Figure 20 shows a diagram of such a cluster source. The aggregation chamber is filled with a cold gas at several mbar. Upon reaching supersaturation and after many collisions within the inert gas, atoms start to nucleate to clusters.[37] The newly formed particles continue to grow either by surface growth or by coagulation, which is the clumping together of separate clusters.[58] The heat of condensation released by the growing cluster is carried away by the carrier gas. Cluster size can be controlled by varying parameters such as aggregation chamber length, carrier gas type and flow rate, sputtering type (DC or RF) and power.[37] The production of the particle beam is very simple: The particles flow through an orifice in a very thin wall of a reservoir, in which the gas is in thermal equilibrium, into the deposition chamber. This opening is small enough so that the outgoing flow will not disturb the equilibrium in the reservoir. The gas stream will expand either sonic or supersonic depending on the pressure ratio inside/outside the reservoir.[58]

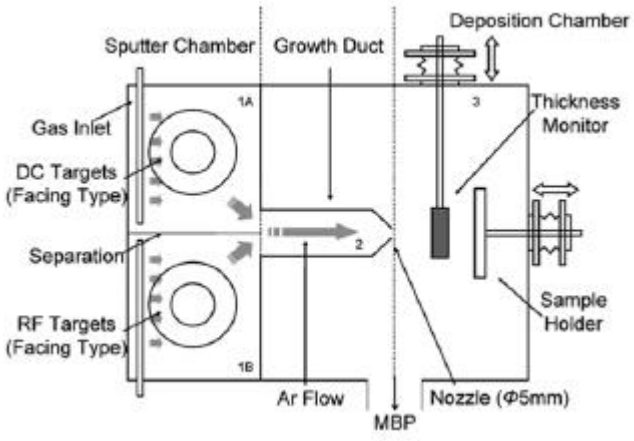

Figure 20 Plasma-gas condensation cluster source[58]

The process of growth of a cluster is a process of constant attachment of atoms to, and evaporation of atoms from the cluster surface. The rates of these processes are connected by the principle of detailed balance, and the equilibrium between a cluster and parent vapor is similar to that between a bulk surface and its parent vapor.[59] The vapor pressure at which the vapor and cluster are in equilibrium (the rate of attachment is equal to the rate of evaporation), is called the saturation

pressure. In a supersaturated gas, the vapor pressure exceeds the saturation pressure. The supersaturation degree is given by

$$S = \frac{N}{N_{sat}}$$ **Equation 9**[59]

Where N is the atom number density of the vapor, and N_{sat} is the atom number density of saturated vapor. Condensation of clusters only takes place if S > 1. For every supersaturation degree, there is a critical cluster size given by

$$n_{crit} = (\frac{\Delta\varepsilon}{T \ln S})^3$$ **Equation 10**[59]

Where n_{crit} is the critical cluster size, Δε is the change in atom binding energy of the cluster, T is temperature and S is supersaturation degree.

The concept of critical size means that for large clusters whose size exceeds the critical size, the probability of atom attachment is larger than the probability of atom evaporation, thus the cluster grows. For cluster with $n<n_{sat}$ this is opposite and such cluster evaporate.[59] The cluster growth is accompanied by a decrease of the number of free atoms, and stops when the size of the clusters corresponds to the critical cluster size at a certain number density of free atoms; the system is in equilibrium.[59]

The law of evolution of the radius of a cluster over time states shows the dependency of the cluster size on the diffusion in the flow gas and on the atom number density:

$$r = \sqrt{\frac{mDNc_{\infty}t}{2\rho}}$$ **Equation 11**[59]

In which m=atomic mass, D=diffusion coefficient, N=atom number density, c_{∞}=atomic concentration far from particle, t=time, ρ=bulk density.

Two clusters can also associate forming one bigger cluster. The number of associating clusters per unit time is given by

$$J = 4\pi\ D\ r\ N_0$$ **Equation 12**[59]

Where D is the diffusion coefficient in the carrier gas, r is the sum of the two associating clusters, and N_0 is the number density of clusters.

Size selection of the produced clusters can be obtained by applying various methods depending on the charge state or mass range of the clusters. Aerodynamic focusing of neutral clusters uses a system of aerodynamic lenses which exploit the difference in radial drag that different sized particles undergo. The outgoing clusters close to the nozzle edge experience the strongest radial drag. Since the radial drag is also size dependent, it can be used for size selection: The inertia of large particles having Stokes number St >> 1 exceeds the drag action of the flow gas and thus will not follow the gas flow, which leads to their deposition on the walls. Very small

particles will follow the turbulent gas flow closely and be trapped in the vortices. The result is that only particles with St ≈ 1 will join the central beam and pass through the lenses (see Figure 21).[37]

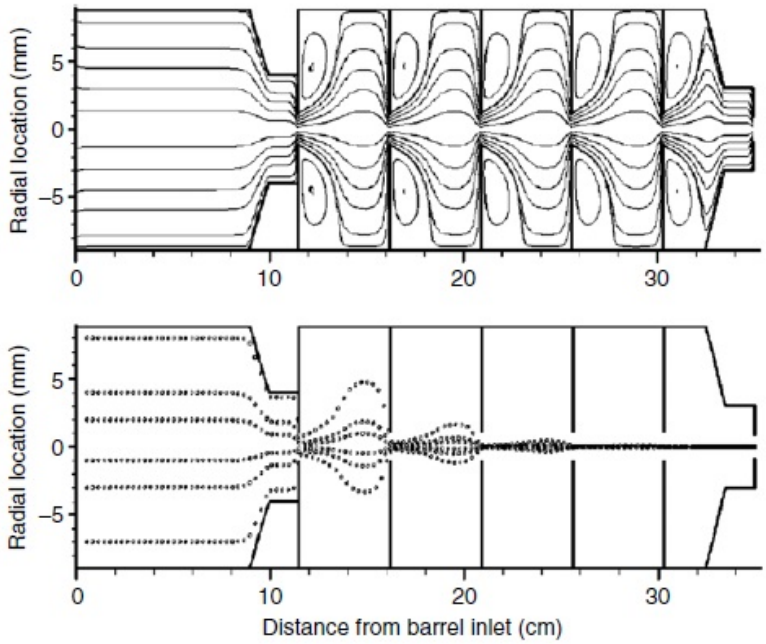

Figure 21 Calculated flow streamlines (top) and particle trajectories (bottom) in the aerodynamic lens assembly [37]

For charged clusters, electric and magnetic fields are used to separate different sized particles based on charge-to-mass ratios. Oft used devices are TOF mass spectrometers, radio frequency quadrupole spectrometers and Wien filters (in order of descending resolution).[37]

3.1.4 Cluster deposition

The kinetic energy E_{kin} of a cluster beam divides the cluster-surface interaction into low- and high-energy categories. An interaction is considered to be low-energy when the kinetic energy per atom E_{at} is below the binding (cohesive) energy of the cluster constituents E_{coh}. This is often called deposition or soft landing and typically doesn't induce cluster fragmentation. [37] If E_{at} exceeds E_{coh} the impact is considered to be high-energy. A few scenarios are then possible.

If E_{at} is only slightly higher than E_{coh}, the cluster is significantly plastically deformed on impact but fragmentation is limited. As E_{at} increases further compared to E_{coh}, this results in cluster decomposition and fragmentation. The cluster fragments can either be backscattered or implanted into the surface. A relatively high E_{kin} can lead to significant erosion of the surface such as sputtering of surface atoms and crater formation.[37]

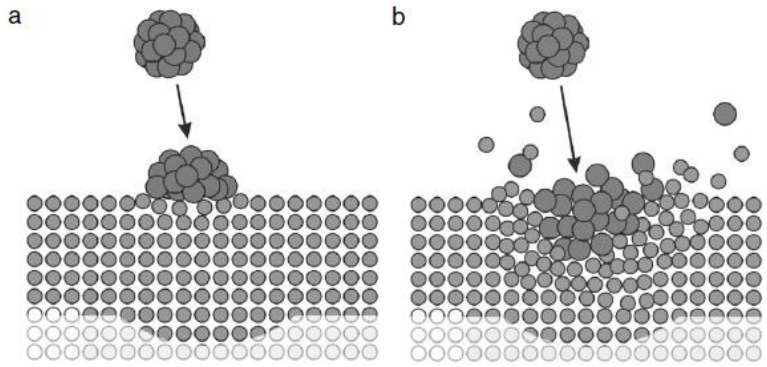

Figure 22 a) cluster soft landing (b) high energy landing [37]

3.2 Installation of cluster source

An Oxford Applied Research NC200U nanoclusters source was installed at the facilities of the Utrecht Solar Energy Laboratory of the Debye Institute of the Utrecht University for use in solar cell applications. Figure 23 gives a schematic diagram of the cluster source apparatus and Table 3 gives an overview of the specifications. The magnetron sputtering system has the option of DC or RF sputtering. The DC power is supplied by a TDK Lambda DC power supply and the RF power by an Oaxial power systems RF generator. Two sputter and aggregation gases can be hooked up (He and Ar), their flow being controlled by MKS instruments mass flow controllers. The sputter gas is injected through a small orifice from the front side of the magnetron gun. 2 inch sputtering targets can be mounted. The system can be either liquid nitrogen or water cooled. The magnetron gun is mounted on a long axial mount, which enables changing the distance between the front of the magnetron gun and the end of the aggregation chamber, thereby effectively changing the aggregation length for the formed clusters. The clusters leave the aggregation region through an exchangeable aperture and an exchangeable cone shaped nozzle. The diameters of both openings can be varied from 4-10 mm. A 520 l/s Balzers turbo pump was mounted to the differential pumping port and keeps the base pressure in the source at 10^{-7} mbar and the operating pressure at about 10^{-4} mbar. The source was mounted on a high vacuum deposition chamber, at first at an angle of approximately 45 degrees with the substrate holder and at a source-target distance of approximately 50 cm. Because only small amounts of clusters were detected on the substrates, the source was mounted on a different vacuum chamber; this time right in front of the substrate holder, with a source-target distance of approximately 25 cm. Substrates were placed in the substrate holder manually, with a load-lock system allowing rapid exchange of the samples. A pneumatic valve can close the opening between the source and the vacuum chamber during sample switching, negating the necessity to switch off the source during sample switching.

The advantage of this setup is in the simplicity: the source is operated at room temperature without the complication of having to heat the target, and there is no extraction unit installed: the pressure gradient between the source chamber and the deposition chamber is what extracts the clusters out of the source and towards the sample holder.

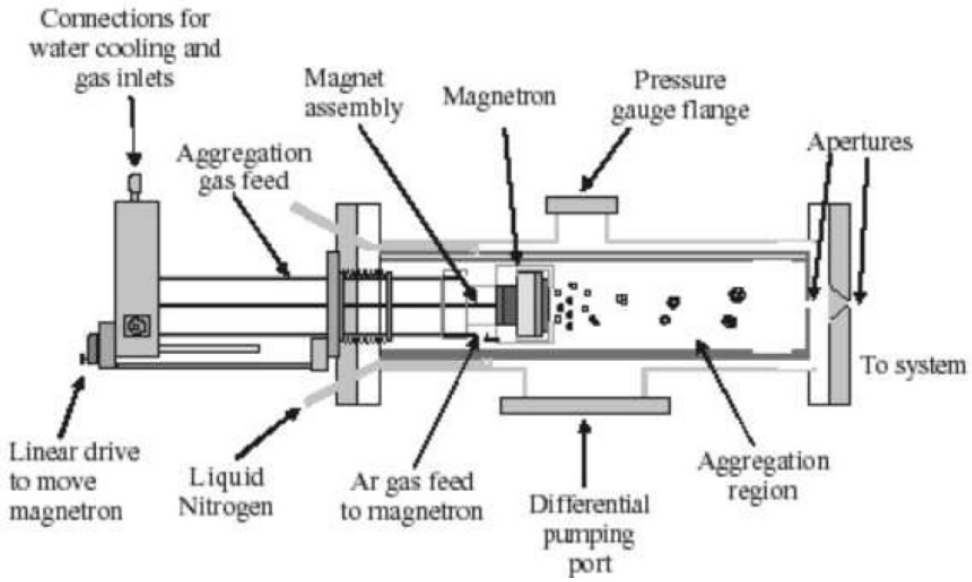

Figure 23 Schematic picture of NCU200U Nanocluster deposition source by Oxford Applied Research as installed

Material Source	1kW DC Magnetron (power supply incl.). Takes 2" diameter targets.
Deposition rate*	<0.001nm/s to ~0.5nm/s
Mean cluster sizes*	<0.4nm to ~10nm in diameter
Ar flow rate required*	10-100sccm
Beam diameter**	5mm to 40mm at a source-sample distance of 100mm
Aggregation length	variable
Source mounting	NW150CF or to customer requirement
Services Required	500l/s differential pumping, 1000l/s pumping on deposition chamber. liq. Nitrogen, Ar gas, up to 2 aggregation gases

Table 3 Specifications of NCU200U Nanocluster deposition source (Oxford Applied Research) *Measurements for Cu using NC200U. Values will depend on material and source parameters. ** Depends on aperture set.

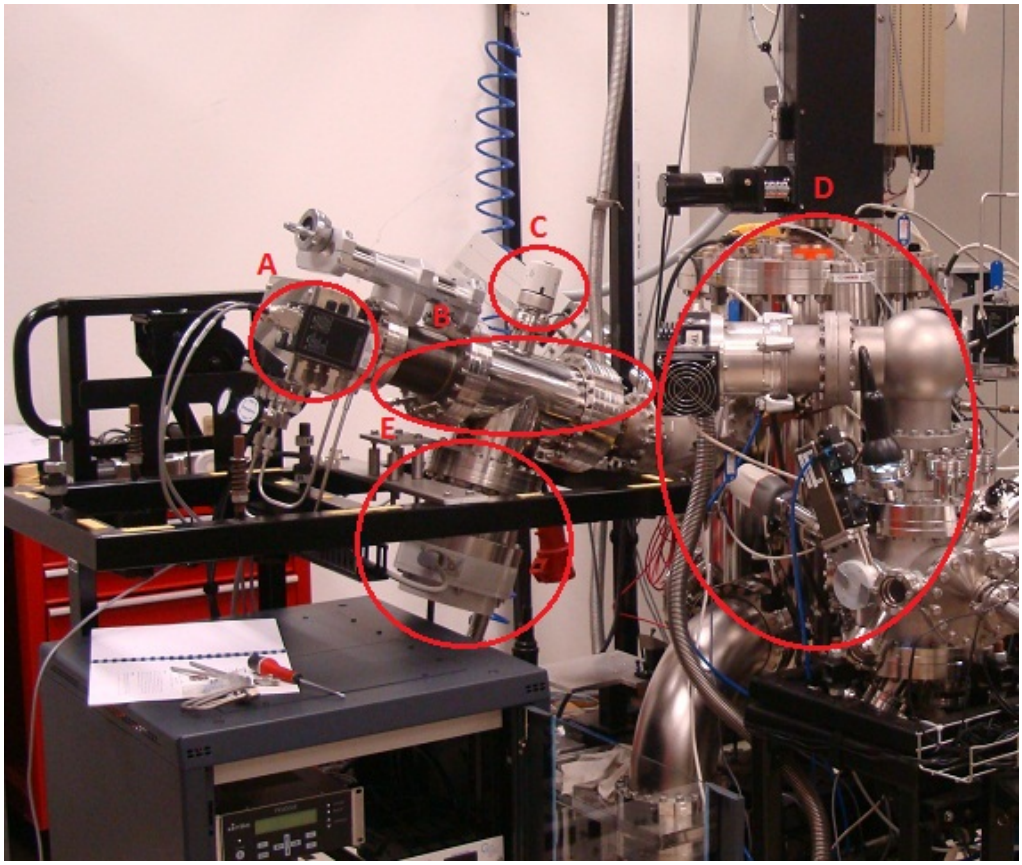

Figure 24 Cluster source mounted to deposition chamber 1. A) Mass flow controllers B) Cluster source C) Pressure monitor D) Deposition chamber 2 E) Turbo pump

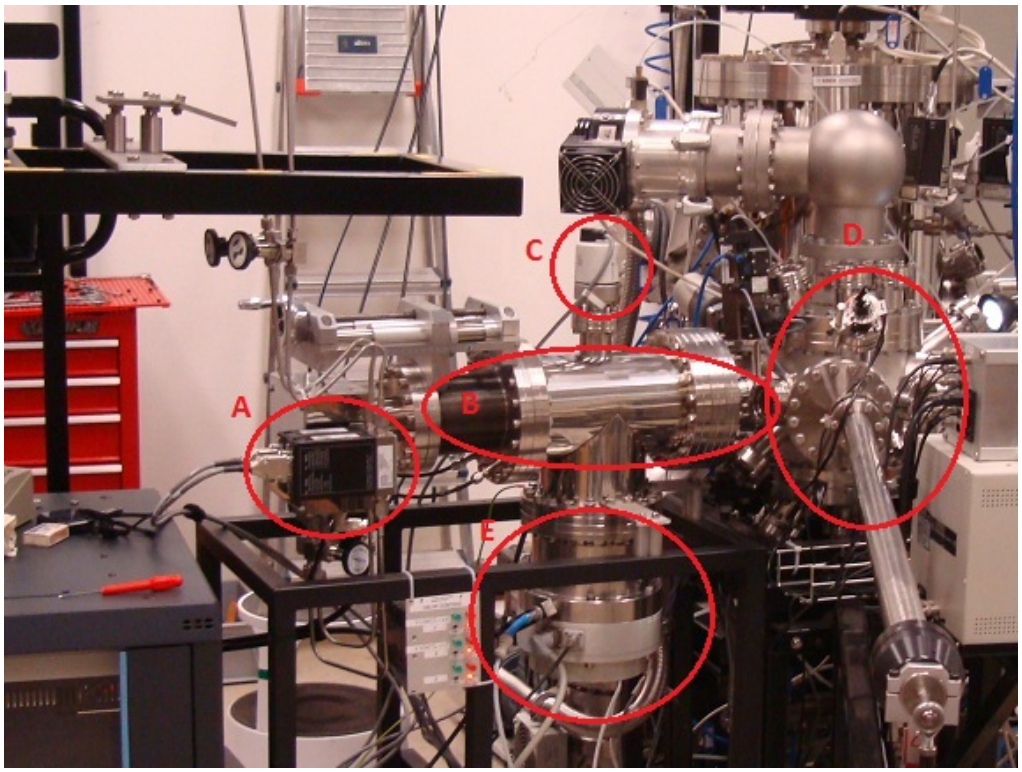

Figure 25 Cluster source mounted to deposition chamber 2. A) Mass flow controllers B) Cluster source C) Pressure monitor D) Deposition chamber 2 E) Turbo pump

Alignment

The alignment of the cluster source beam with the substrate holder was a crucial part of the installation process. Especially since the distance between the exit of the source and the substrate holder was substantial (50 cm) for the first position in which the source was mounted, the number of cluster hitting the substrate was relatively small because of fanning out of cluster beam and because of the angle with which the beam hit the substrate. Before aligning, a 10x10cm glass plate was mounted in front of the substrate holder to check if the where the beam was located. Figure 26 shows the glass plate after a deposition with Ag clusters. The black dot at the right bottom corner represents the spot of the substrate holder. It can be seen that it is located at the edge of the cluster beam. Since the cluster source was mounted on a frame which could be adjusted in height as well as laterally, and because the source was connected to the deposition chamber with a flexible piece, aligning could be done fairly easily by adjusting the position of the cluster source. By connecting a picoammeter to the substrate holder, the current caused by charged clusters hitting the substrate could be measured. Maximizing this current by adjusting the position of the source was the tool used to align the beams maximum intensity on the substrate.

Figure 26 Glass plate after deposition to check alignment of cluster beam on substrate. The black dot represents the location of the substrate

3.3 Operating conditions

3.3.1 Sputter power

Both DC and RF power sources were used. The DC power source was a TDK Lambda DC source and the RF power source an Oaxial power systems RF generator. DC power was varied by adjusting the current in the range 0,100 A-0,350 A. Voltage varied in the range 270 V-385 V. The power ranged accordingly by 27 W-136 W.

RF power was varied in the range 40 W-90 W, with a bias voltage range of -193 V- -247 V.

3.3.2 Aggregation length

The length of the aggregation chamber could be adjusted manually without venting the cluster source over a range of 70 mm.

3.3.3 Flow gas

Argon was used as the sputter gas and as the flow gas for all of the deposition. The Ar flow was controlled by a MKS mass flow controller, and ranged from 10 sccm to 40 sccm. The maximum gas flow was limited by the pump, which produced excess heat at higher flows.

3.3.4 Cooling

Cooling water was used to cool the magnetron and the aggregation chamber for all depositions, to extract the excess heat and maintain a level temperature during the depositions. The option of using liquid nitrogen as a coolant was not used. Cooling water was not turned off when cluster source was idle.

3.3.5 Pressures

Table 4 gives an overview of typical base and operating pressures for the cluster source and the deposition chambers.

Chamber	Base pressure (mbar)	Operating pressure (mbar)
Cluster source	2 E-07	3 E-03
Deposition chamber 1	5.5 E-08	2 E-05
Deposition chamber 2	2.5 E-05	5.5 E-05

Table 4 Overview of typical pressures of the different chambers before and during deposition

3.3.6 Deposition chambers

Deposition chamber 1 was a stainless steel cylindrical chamber with a height of 80 cm and a radius of 20 cm. It had a single substrate holder, in which the substrate could be placed manually using a lever-system. The substrate is placed 50 cm from the cluster source orifice. The cluster beam made an angle of approximately 45 degrees with the substrate holder.

Deposition chamber 2 was a stainless steel cylindrical chamber with a height of 20 cm and a radius of 10 cm. It had 12 substrate holders on a carrousel. The substrate is placed 25 cm from the cluster source orifice. Figure 27 shows a schematic diagram of the setup.

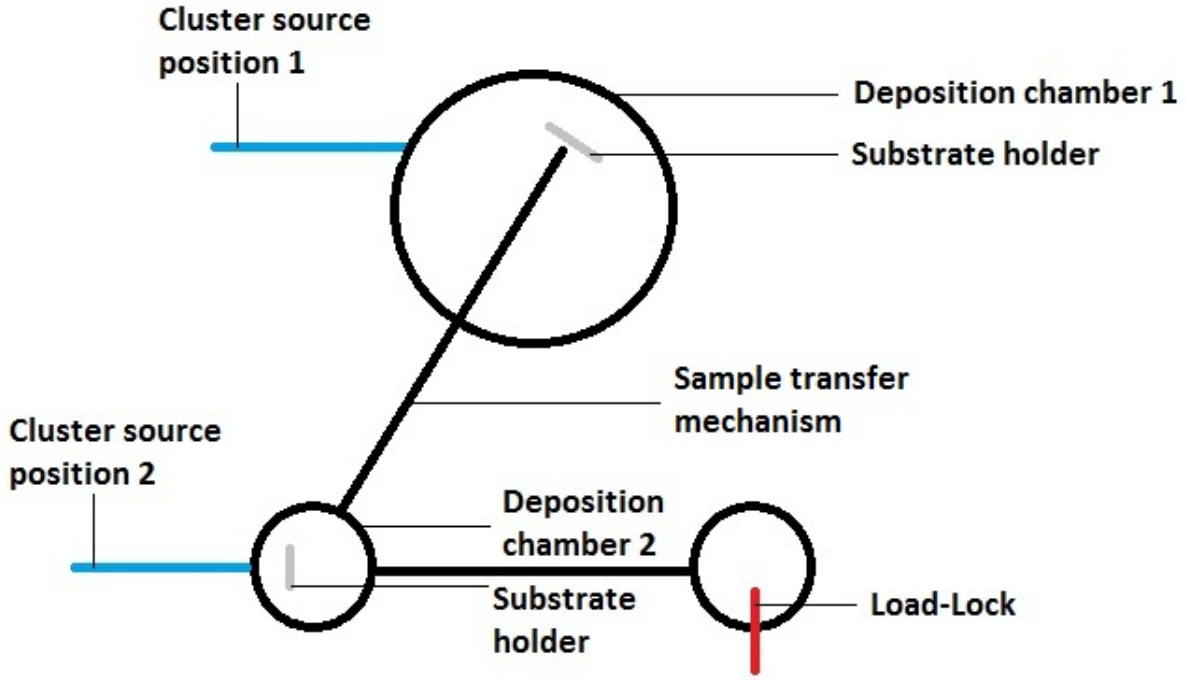

Figure 27

3.3.7 Substrate holder

Figure 28 shows a substrate holder with a 1x1 cm glass substrate. Substrates were held in place by a clamp on the backside and transferred from the lock-load chamber to the deposition chambers manually.

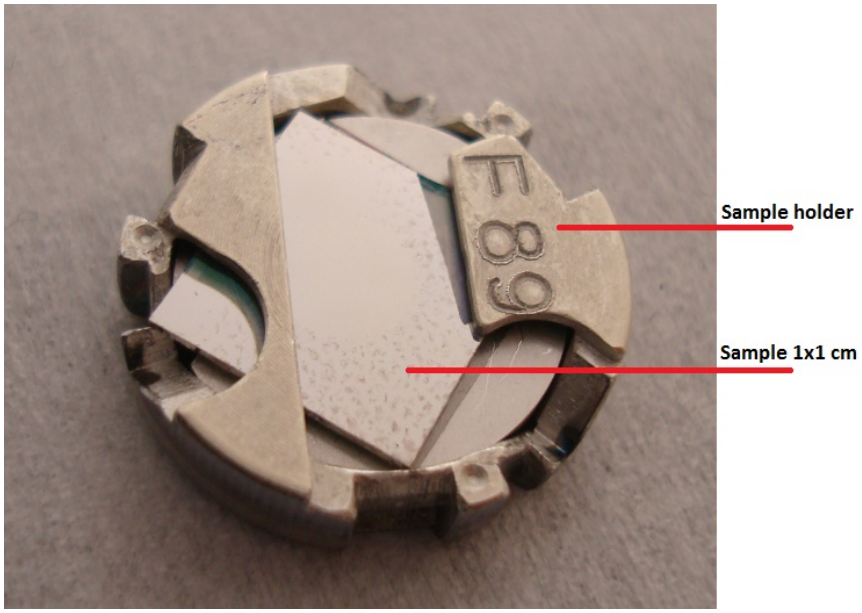

Figure 28 Substrate holder with a 1x1 cm substrate

3.4 Reproducibility

Except for the abovementioned factors influencing the cluster size and sputtering rate (aggregation chamber length, carrier gas type and flow rate, sputtering type (DC or RF) and power), there are a number of factors influencing the cluster production, making the reliability of this type of cluster source somewhat problematic. Deformation of the target surface can influence the cluster size distribution: a new, smooth target produces smaller clusters than when the target is eroded.[60] After the target has been used for a period of time, the thinning of the target causes the magnetic field to increase, resulting in a higher sputtering rate. If the trench in the target becomes deeper than half the target thickness, the plasma gets distorted which weakens the sputtering. There is a trade-off between the two effects, with the latter having a greater impact as the trench deepens.[60]

Figure 29 shows another issue affecting the reproducibility. As can be seen, the peak of the mass of the clusters that are being produced shifts to a lower value as the cluster source is discharging for a prolonged period of time. These are data for Cu clusters produced by a similar cluster source setup as used for this research.[61] As the discharge time of the source increases, so does the temperature of the aggregation chamber, which might explain the shift in cluster size.[61]

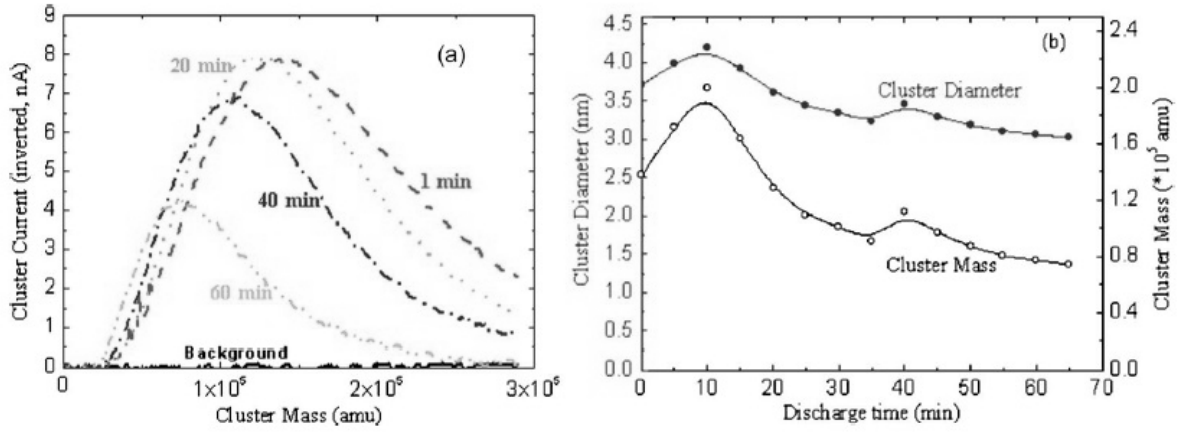

Figure 29 Quadrupole mass spectrum analysis of Cu nanoclusters. (a) Variation of cluster mass and cluster current (b) reproducibility of cluster diameter (nm) and cluster mass with discharge time[61]

3.5 Analysis of samples

Analysis of the samples was performed using Atomic Force Microscopy (AFM). The AFM set-up is a Nanoscope(R) IIIa (Digital Instrum ents, Santa Barbara, CA) system equipped with E-scanner and has been used in the tapping mode. Images produced were further analyzed using Gwyddion 2.28. Only height data have been used for the analysis, since the width of the clusters isn't reliable due to tip convolution of the AFM measurements.

3.6 Examples of deposited clusters

Clusters of silicon, silver and germanium were deposited with the cluster source setup. All clusters were produced while keeping the settings well within limits of material maxima, according to the equipment's manual.

3.6.1 Si clusters

Si clusters were deposited on 1x1 cm 100 silicon wafer substrates. Both DC and RF were used to produce the clusters. For the deposition of Si clusters, the clusters source was mounted to deposition chamber 2 (see section 3.3.6 for details).

Figure 30 and Figure 31 show 2D and 3D pictures of DC sputtered clusters after a 30 minute deposition with DC voltage 345 V, DC current 0.2 A, Ar flow 35 sccm and aggregation length 45 mm. The clusters are spread evenly over the sample with no visible aggregates. The height of the clusters ranges from 2.4 to 5.6 nm, with an average value of 3.5 nm. Figure 32 shows the height distribution of the Si clusters in the AFM image. Clusters smaller than 2.4 nm could not be detected because of background noise.

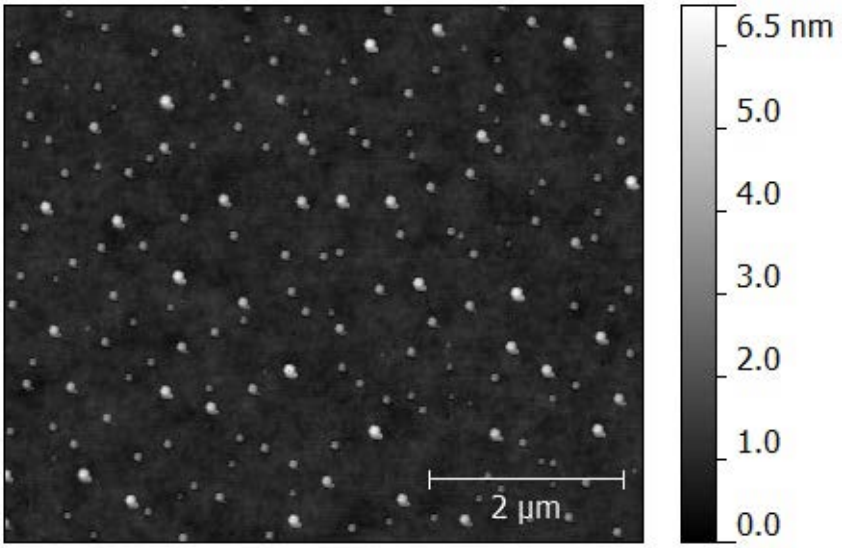

Figure 30 2D AFM image of Si DC sample after 30 minutes deposition with P = 69 W, L agg = 45 mm, Ar flow = 35 sccm

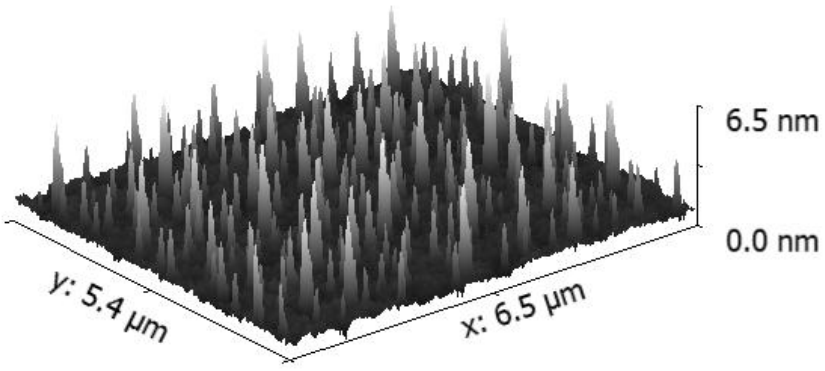

Figure 31 3D AFM image of Si DC sample after 30 minutes deposition with P = 69 W, L agg = 45 mm, Ar flow = 35 sccm

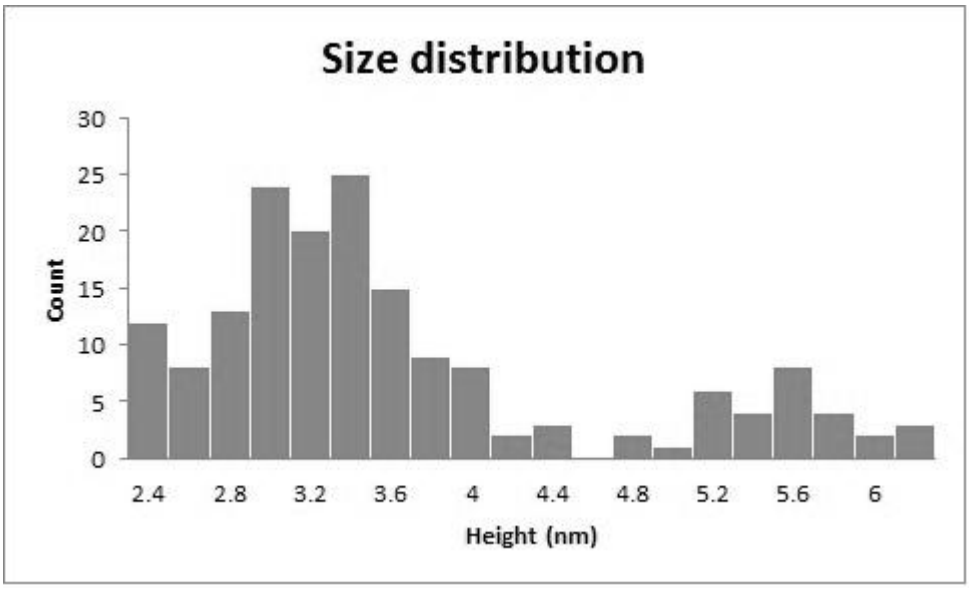

Figure 32 Size distribution of Si clusters on sample after 30 minutes DC deposition with P = 69 W, L agg = 45 mm, Ar flow = 35 sccm

Figure 33 and Figure 34 show 2D and 3D AFM pictures of RF sputtered clusters after a 30 minutes deposition with RF forwarded power 90 W, bias voltage -247 V, Ar flow 20 sccm, and an aggregation length of 45 mm. The clusters are spread very evenly over the sample, without any visible aggregates. The height of the clusters ranges from 3.5 nm to 13.5 nm with an average of 5.3 nm. Figure 35 shows the height distribution of the Si clusters in the AFM image. Clusters smaller than 3.5 nm could not be detected because of background noise.

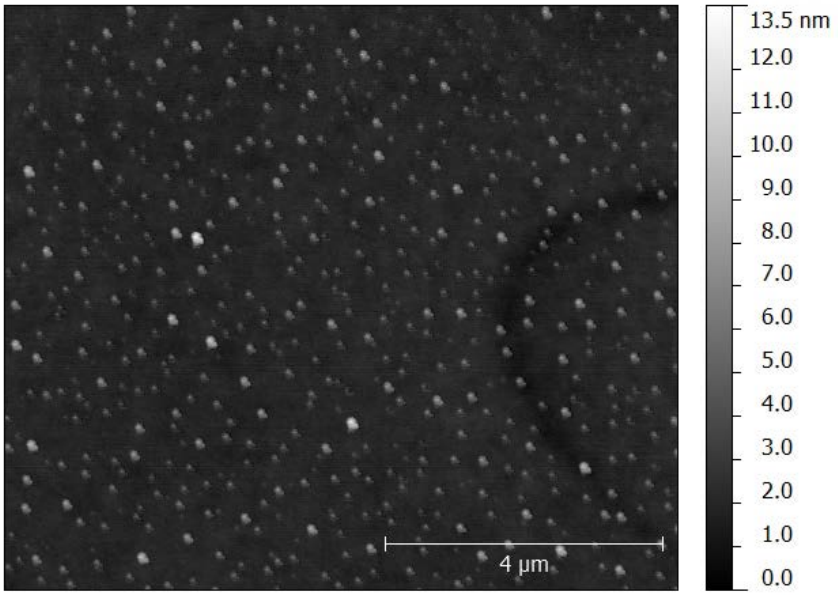

Figure 33 2D AFM image of Si RF sample after 30 minutes deposition with P = 90 W, L agg = 45 mm, Ar flow = 20 sccm

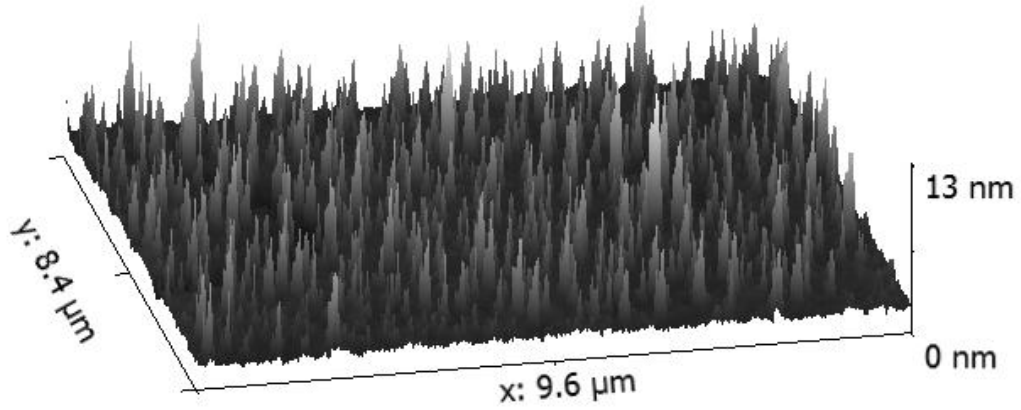

Figure 34 3D AFM image of Si RF sample after 30 minutes deposition with P = 90 W, L agg = 45 mm, Ar flow = 20 sccm

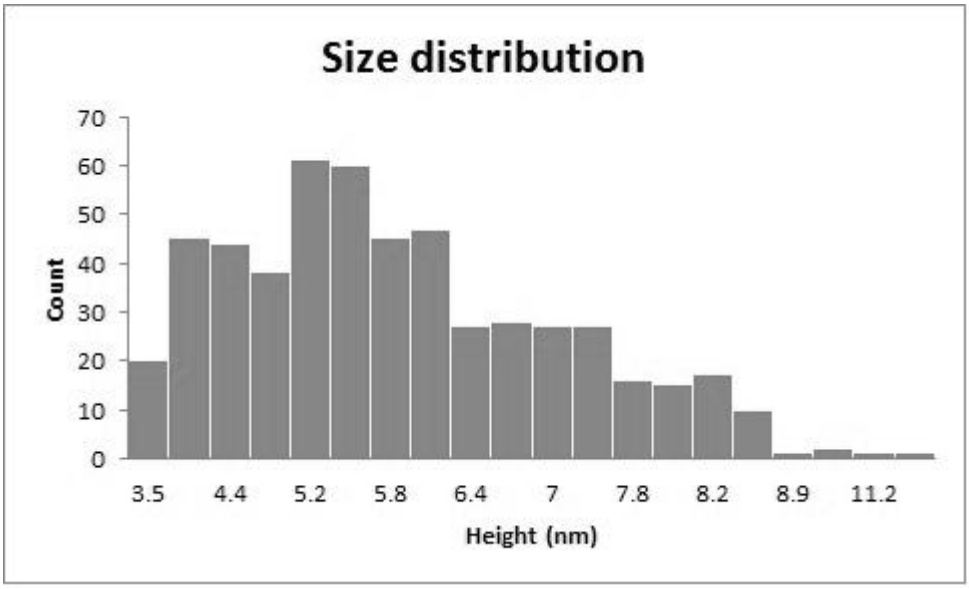

Figure 35 Size distribution of Si clusters on sample after 30 minutes RF deposition with P = 90 W, L agg = 45 mm, Ar flow = 20 sccm

3.6.2 Ag clusters

Silver clusters were deposited on 1x1 cm glass substrates. Both RF and DC sputtering were used to produce the clusters. For the Ag cluster deposition, the cluster source was mounted to deposition chamber 1 (see section 3.3.6 for details).

Figure 36 and Figure 37 show 2D and 3D pictures of DC sputtered clusters after a 5 minute deposition with DC voltage 266 V, DC current 0.083 A, Ar flow 17 sccm and aggregation length 50 mm. The clusters are spread evenly over the sample and have a circular base, although the diameter is much larger than the height. A variation in size of the clusters is visible. The height of the clusters ranges from 4.4 to 18.6 nm with an average value of 6.5 nm. Figure 38 shows the height distribution

of the Ag clusters in the AFM image. Clusters smaller than 4.8 nm could not be detected because of background noise.

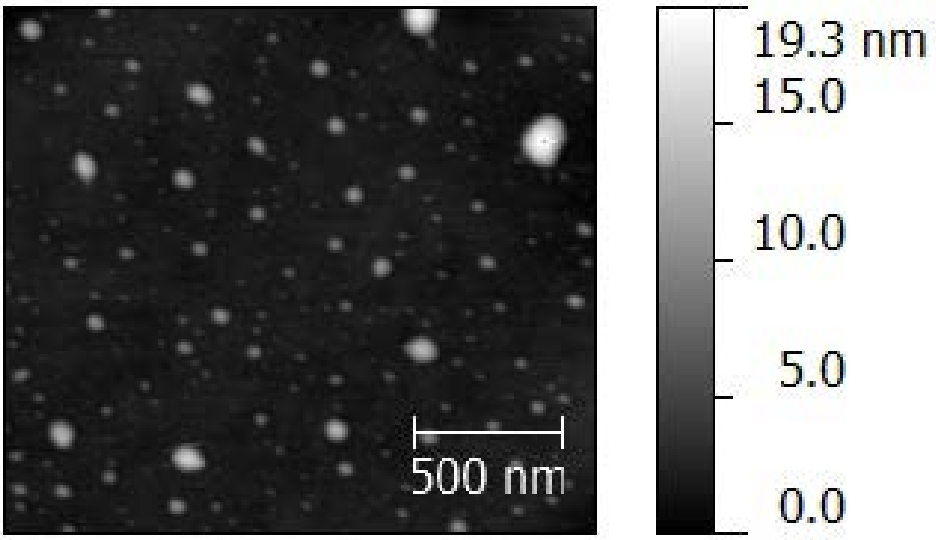

Figure 36 2D AFM image of Ag DC sample after 5 minutes deposition with P = 22 W, L agg = 50 mm, Ar flow = 18 sccm

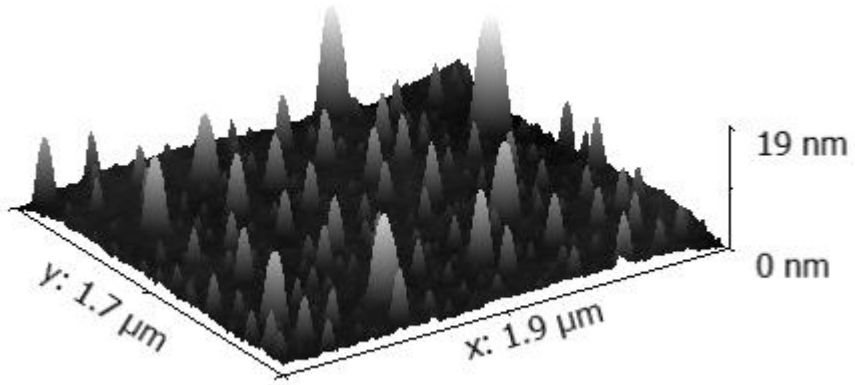

Figure 37 3D AFM image of Ag DC sample after 5 minutes deposition with P = 22 W, L agg = 50 mm, Ar flow = 18 sccm

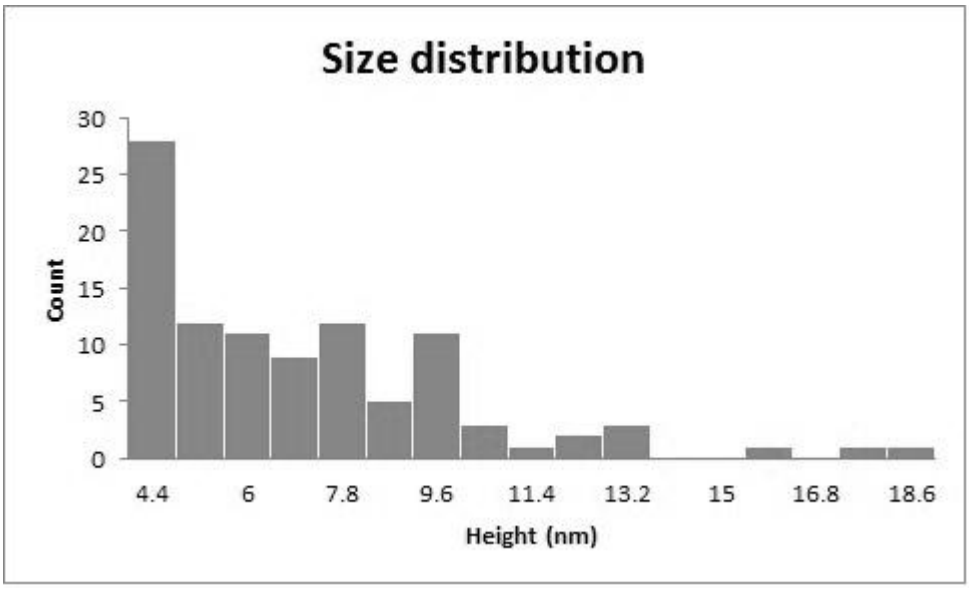

Figure 38 Size distribution of Ag clusters on sample after 5 minutes DC deposition with P = 22 W, L agg = 50 mm, Ar flow = 18 sccm

Figure 39 and Figure 40 show 2D and 3D AFM pictures of RF sputtered clusters after a 10 minutes deposition with RF forwarded power 60 W, bias voltage -216 V, Ar flow 15 sccm, and an aggregation length of 77 mm. The clusters are less evenly spread over the sample than the DC clusters. Most clusters are spherical, but some are shape irregularly, possibly through aggregation. The height ranges from 3.8 nm to 14.1 with an average height of 6.3 nm. Figure 41 shows the height distribution of the Ag clusters in the AFM image. Clusters smaller than 3.8 nm could not be detected because of background noise.

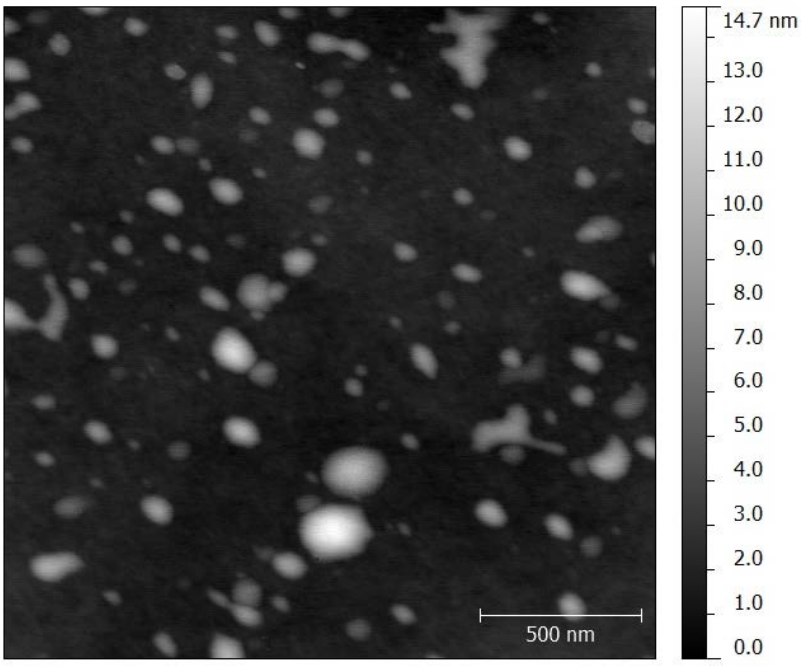

Figure 39 2D AFM image of Ag RF sample after 10 minutes deposition with P = 60 W, L agg = 77 mm, Ar flow = 15 sccm

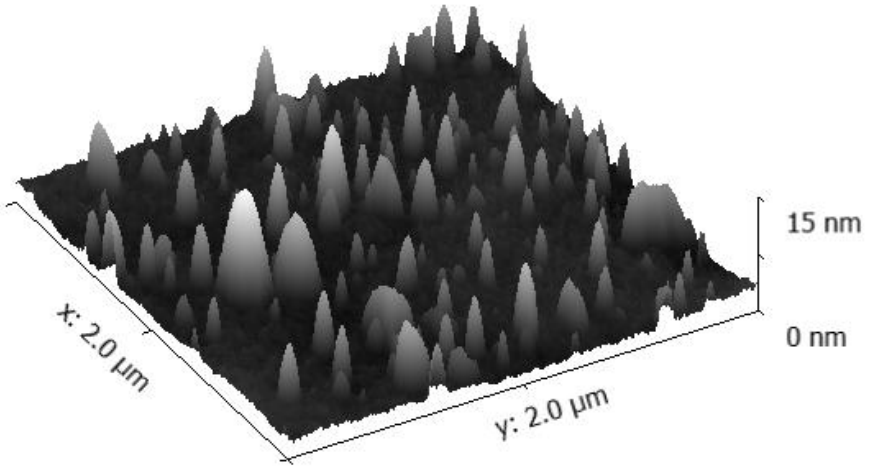

Figure 40 3D AFM image of Ag RF sample after 10 minutes deposition with P = 60 W, L agg = 77 mm, Ar flow = 15 sccm

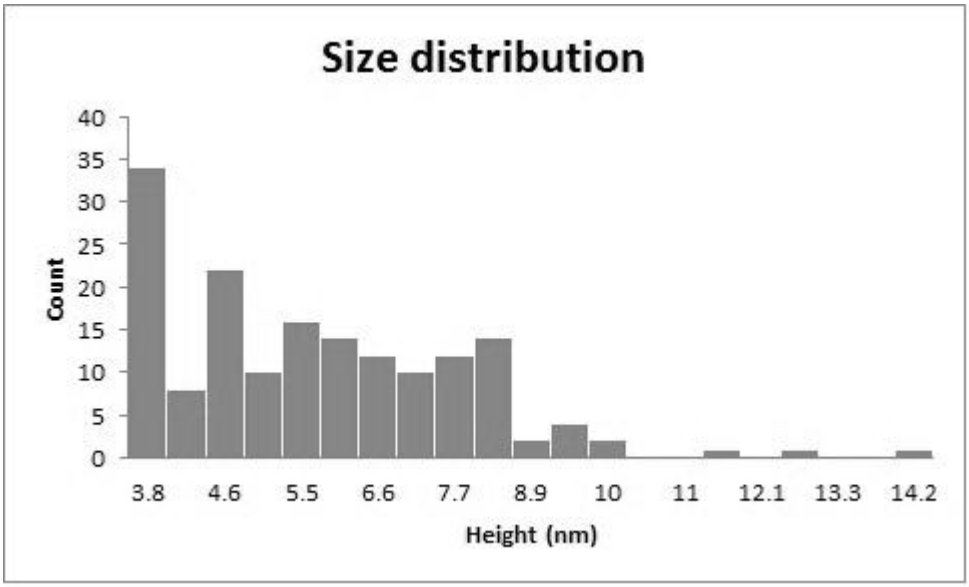

Figure 41 Size distribution of Ag clusters on sample after 10 minutes RF deposition with P = 60 W, L agg = 77 mm, Ar flow = 15 sccm

Figure 42 is a TEM image of DC sputtered clusters after a deposition of 10 minutes with DC voltage 270 V, DC current 0.097 A, Ar flow 18 sccm and aggregation length 100 mm. The average diameter of the clusters on this sample is 10.1 nm, which is much smaller than the diameter seen in the AFM images where the diameter is typically > 100 nm. Due to tip convolution the diameter measured in the AFM images is less reliable, but hitting the hard glass or silicon surface of the substrates used for AFM analysis could deform the cluster.

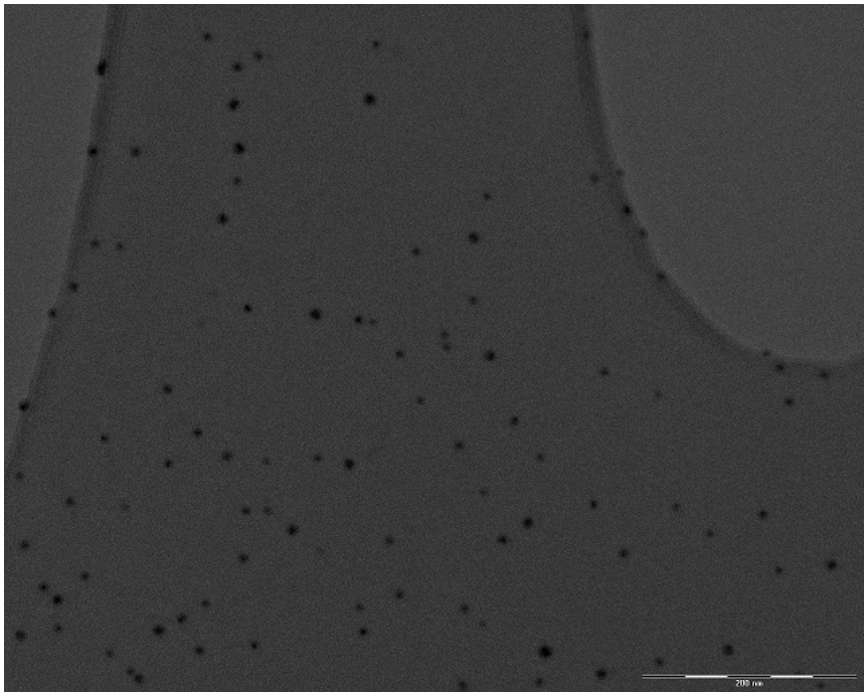

Figure 42 TEM image of Ag DC sample after 10 minutes deposition with P = 28 W, L agg = 100 mm, Ar flow = 18 sccm

3.6.3 Ge clusters

Germanium clusters were produced on 1x1 cm 100 silicon wafer substrates. DC sputtering was used to produce the clusters. For deposition of Ge clusters deposition chamber 2 was used (see section 3.3.6). Figure 43 and Figure 44 show 2D and 3D pictures of DC sputtered clusters after a 120 minute deposition with DC voltage 317 V, DC current 0.2 A, Ar flow 30 sccm and aggregation length 32 mm. Even though the deposition time was 120 minutes, only a few clusters were visible on the substrate. The height of the clusters varied from 2.1 nm to 4.2 nm with an average of 2.8 nm. Figure 45 shows the height distribution of the Ge clusters in the AFM image. Clusters smaller than 2.1 nm could not be detected because of background noise.

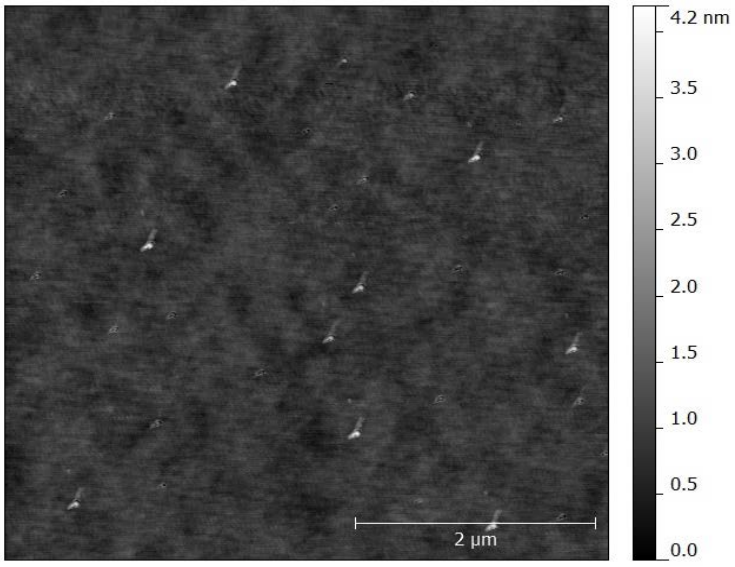

Figure 43 2D AFM image of Ge DC sample after 120 minutes deposition with P = 63 W, L agg = 32 mm, Ar flow = 30 sccm

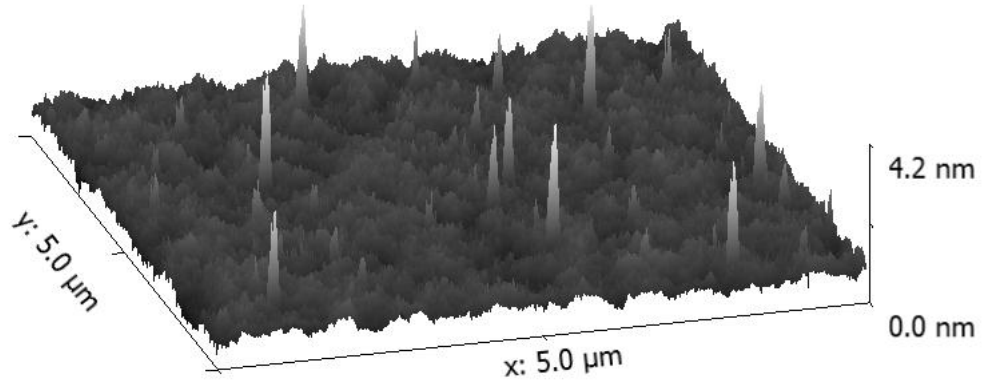

Figure 44 3D AFM image of Ge DC sample after 120 minutes deposition with P = 63 W, L agg = 32 mm, Ar flow = 30 sccm

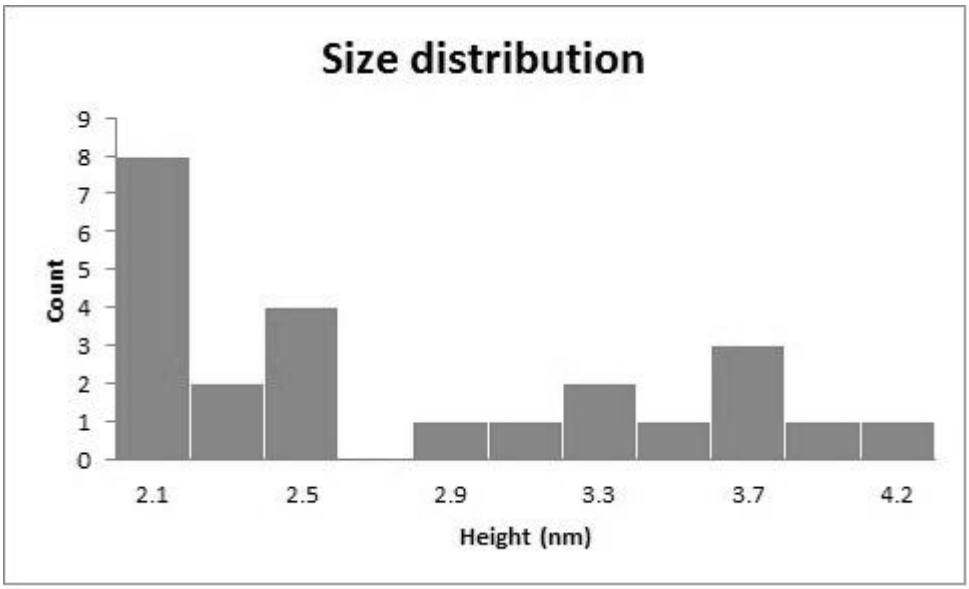

Figure 45 Size distribution of Ge clusters on sample after 120 minutes DC deposition with P = 63 W, L agg = 32 mm, Ar flow = 30 sccm

3.7 Characterization and analysis

3.7.1 Reproducibility

When analyzing the results of the characterization, an important side note is the aforementioned reproducibility problems of this type of cluster source setup. Comparing samples and series of samples with one another is only possible if the results are reliable and reproducible. Table 5 shows the details of 3 Si cluster samples produced under the same DC operating conditions of the cluster source. For all three samples, the average cluster height is very comparable. The cluster density however varies greatly. These results show that the average cluster height is a reproducible and thus reliable measure, while the cluster density is not.

Sample	L aggr (mm)	Ar flow (sccm)	P (W)	Cluster density (clusters/um2)	Height avg (nm)
C67 avg	45	30	68.5	16.50	2.71
C71.000	45	30	68.6	18.5	2.7
C81 avg	45	30	69.5	1.8	2.8

Table 5 Results of 3 different Si cluster samples produced with DC sputtering the same settings

3.7.2 Si clusters

An extensive characterization of the cluster source was performed to gain further insight in the cluster source mechanisms and how the factors aggregation length, magnetron power, and Ar flow rate influence the rate of cluster deposition and the size of produced clusters. By changing one variable and keeping the other variables constant, the influence of the changing variable was established.

Aggregation length

The aggregation length was varied in steps of 15 mm, from the minimum of 30 mm to the maximum of 99 mm. The Ar flow and magnetron power were kept constant at 30 sccm and 68 W respectively. Figure 46 A and B show the dependence of the average cluster height and cluster density on the aggregation length. Table 6 gives an overview of the relevant values.

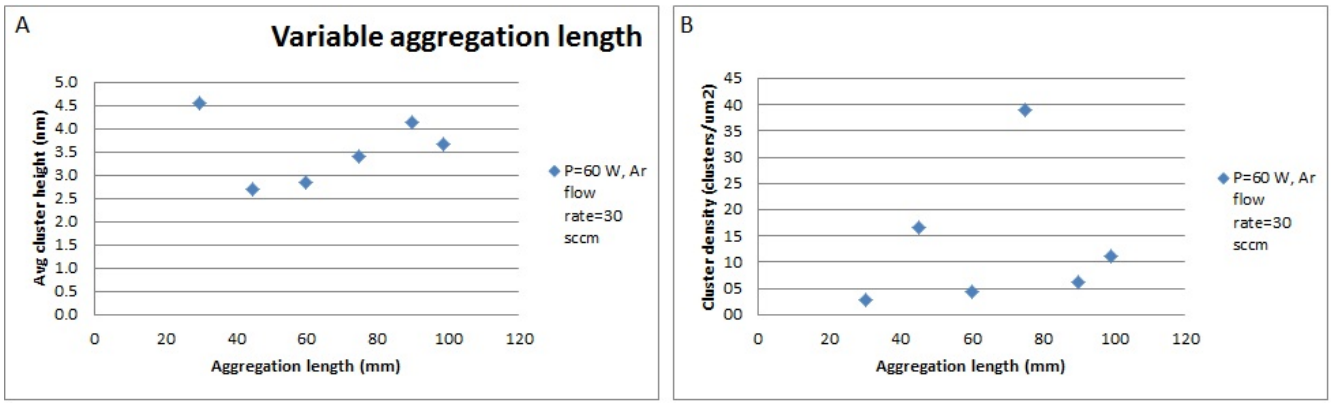

Figure 46 A) graph of average cluster height vs aggregation length B) graph of cluster density vs aggregation length

Sample ID	L aggr (mm)	Ar flow (sccm)	P (W)	Cluster density (clusters/µm^2)	Height avg (nm)
C62	30	30	68	2.8	4.6
C67	45	30	69	16.5	2.7
C66	60	30	68	4.4	2.9
C65	75	30	68	39.0	3.4
C64	90	30	68	6.2	4.1
C63	99	30	68	11.1	3.7

Table 6 Overview of values for DC sputtered Si cluster series with variable aggregation length

Figure 46 shows how the average cluster height and cluster density depend on the aggregation length. Except for sample C62 (aggregation length 30 mm), a visible trend is that average cluster height increases for larger aggregation lengths, which is to be expected since cluster stay in the aggregation chamber for a longer time and have more time to grow. Since the sample C62 was the first produced in the series, this could explain the larger value for the cluster height, as the deposition conditions might not have stabilized fully. The cluster density for sample C62 is low, meaning that there were only a few clusters visible on the sample. Smaller clusters may have aggregated, forming the larger structures that were measured with the AFM and thereby reducing overall cluster density.

The trend that a larger aggregation length produces larger clusters is expected: the larger aggregation length allows the clusters to undergo more collisions and thus they're likely to grow larger.

Cluster density varies with different aggregation lengths, but no clear trend can be identified.

Ar flow rate

The Ar flow rate was varied from 15 to 35 sccm in steps of 5 sccm. The maximum flow rate was limited by the capacity of the pump attached to the cluster source. The aggregation length and magnetron power were kept constant at 45 mm and 70 W respectively.

Figure 47 A and B show the dependence of the average cluster height and cluster density on the Ar flow rate. Table 7 gives an overview of the relevant values.

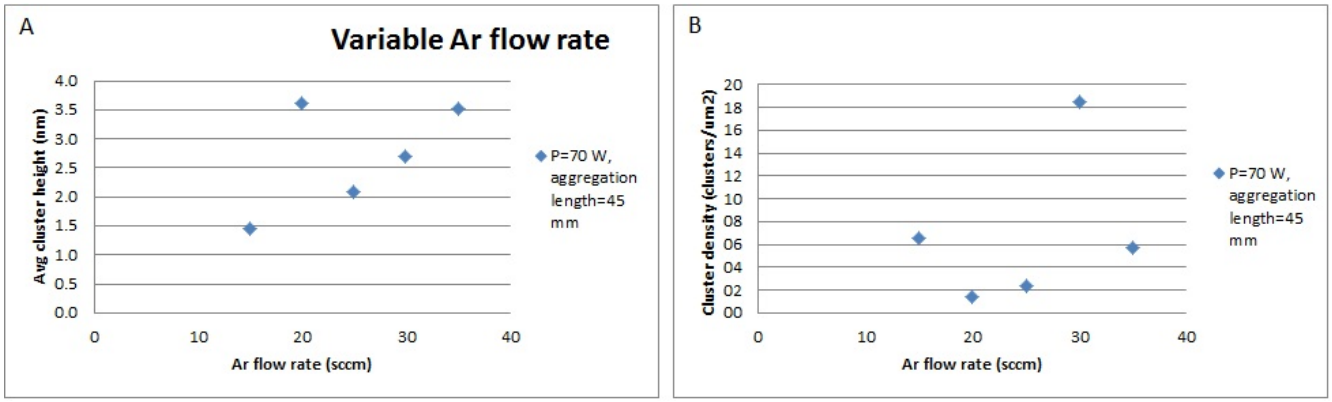

Figure 47 A) graph of average cluster height vs Ar flow rate B) graph of cluster density vs Ar flow rate

Sample ID	L aggr (mm)	Ar flow (sccm)	P (W)	Cluster density (clusters/µm^2)	Height avg (nm)
C68	45	15	72	6.5	1.5
C69	45	20	71	1.4	3.6
C87	45	25	70	2.3	2.1
C71	45	30	69	18.5	2.7
C88	45	35	69	5.7	3.5

Table 7 Overview of values for DC sputtered Si cluster series with variable Ar flow rate

When looking at Figure 47A, the average cluster height increases with increasing Ar flow rate, with the exception of sample C69 (flow rate 20 sccm). The cluster density for C69 is very low, which could mean that several smaller clusters have aggregated to form bigger ones. As clusters aggregate to form one larger particle, the density of cluster decreases while the average size increases. This explains the high cluster height and the low cluster density for C69.

There can be several explanations for the larger clusters with a larger Ar flow. The plasma might be affected by the larger Ar flow, making sputtering more effective. The pressure in the aggregation chamber is increased, which might stimulate aggregation through more collisions of the silicon particles.

Cluster density varies with different aggregation lengths, but no clear trend can be identified.

Magnetron power

The DC magnetron power was varied from 52 to 133 W, with steps of approximately 20 W. The aggregation length and Ar flow rate were kept constant at 45 mm and 30 sccm respectively. Figure 48 shows the dependence of the average cluster height and cluster density on magnetron power. Table 8 gives an overview of all the relevant values.

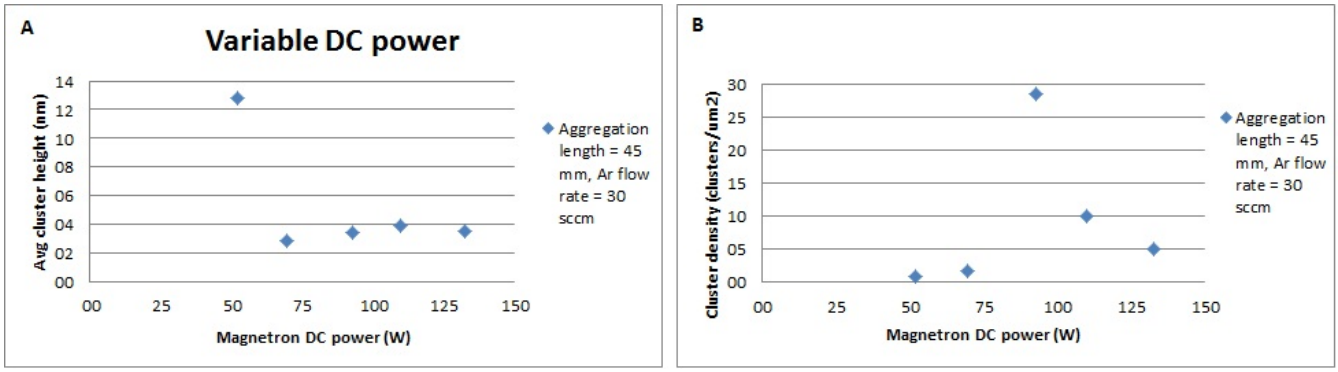

Figure 48 A) graph of average cluster height vs magnetron power (DC) B) graph of cluster density vs magnetron power (DC)

Sample ID	L aggr (mm)	Ar flow (sccm)	P (W)	Cluster density (clusters/µm^2)	Height avg (nm)
C80	45	30	52	0.9	12.8
C81	45	30	70	1.8	2.8
C85	45	30	93	28.5	3.4
C83	45	30	110	10.1	3.9
C86	45	30	133	5.0	3.6

Table 8 Overview of values for DC sputtered Si cluster series with variable magnetron power

Figure 48A shows the dependence of average cluster height on the magnetron power. Sample C80 shows big aggregates of clusters. Smaller clusters have aggregated to form large structures resulting in a very high average height and very low cluster density.

The other samples show an increase in average cluster height from 2.8 nm to 3.6 nm for an increase in power from 70 W to 110 W, after which the average height decreases to 3.6 nm for 133 W. This last decrease might mean there is an optimum for the cluster height between a power of 93 W and 133 W, or this might just be coincidence or an erroneous measurement. More samples in the interval will have to be produced to determine this.

The cluster density shows a clear peak for a magnetron power of 93 W. There might be an optimum for cluster production near this value, but more samples have to be produced to determine this.

RF magnetron sputtering

A short study of the effect of RF magnetron power on cluster production and height has been performed. Figure 49 and Table 9 show the results of this study, which comprised 3 samples.

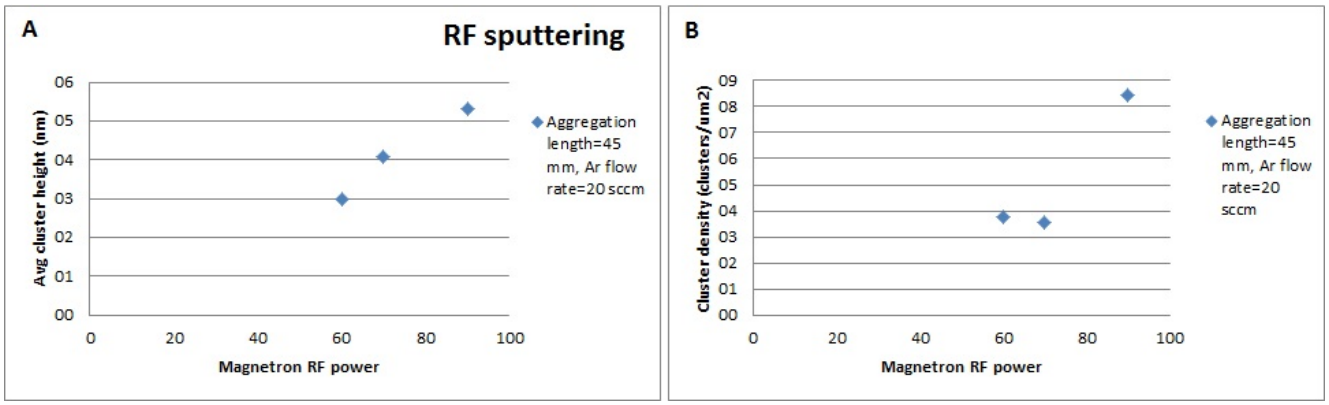

Figure 49 A) graph of average cluster height vs magnetron power (RF) B) graph of cluster density vs magnetron power (RF)

Sample ID	L aggr (mm)	Ar flow (sccm)	P forward (W)	Cluster density (clusters/um2)	Height avg (nm)
C91	45	20	60	3.8	3.0
C90	45	20	70	3.6	4.1
C92	45	20	90	8.4	5.3

Table 9 Overview of values for RF sputtered Si cluster series with variable magnetron power

It is clear that a higher RF power produces cluster with a larger average height. The cluster density is comparable for a power of 60W and 70W, but almost doubles for a power of 90W. As these conclusions are based on only three samples, more samples have to be produced and analyzed to determine the relationship between these values with more certainty. Samples with varying aggregation length that were produced are omitted because AFM image quality was insufficient for analysis.

Dust analysis

Since most of the produced clusters never leave the cluster source but settle on the walls, the dust on the inside of the aggregation chamber was collected and dispersed in isopropanol for analysis. The dispersion was left to settle for a few days, after which a UV-Vis absorption spectrum was made using a Perkin-Elmer Lambda 900 spectrometer. Another absorption spectrum was made after homogenizing the dispersion. The results are shown in Figure 50. An absorption peak is seen at approximately 500 nm, which corresponds to 2.48 eV. The bandgap of bulk Si and Ge is 1.11 eV and 0.67 eV respectively. Decreasing the size of a QD to below the exciton Bohr radius widens the bandgap. So for the absorption peak at 2.48 eV to be anointed to Si or Ge particles, these would have to be well below their respective exciton Bohr radius, which is ~5 nm for Si and ~18 nm for Ge. Further research is needed draw any definitive conclusions.

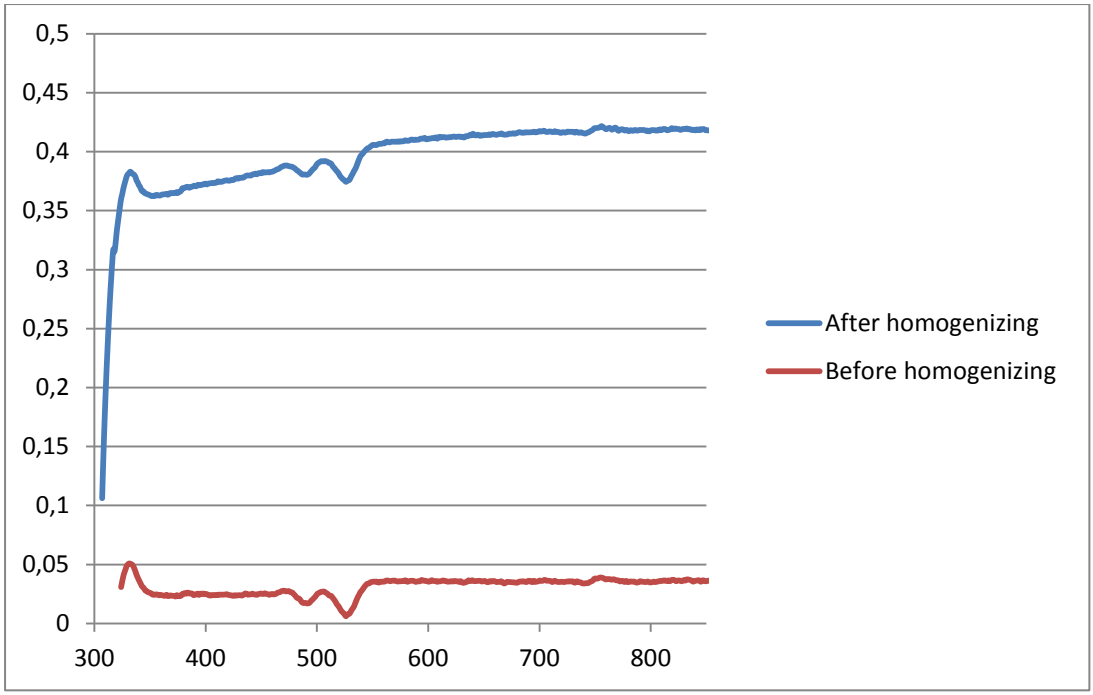

Figure 50 UV-Vis spectrography of Si and Ge dust from aggregation chamber of cluster source

3.7.3 Ag clusters

Of the 4 RF samples and 3 DC samples that were produced during this research, only 1 RF and 1 DC sample gave adequate AFM pictures suitable for analysis. Therefore the comparison between RF and DC deposition of Ag clusters is based on just 1 sample each and no definite conclusions can be drawn.

When comparing the two samples, it stands out that the cluster density (number of clusters per nm^2) is higher for the DC sample (47 clusters/nm^2 DC vs 30 clusters/nm^2 RF), while the deposition time was only halve as long (5 minutes DC vs 10 minutes RF) and the DC power was smaller than the RF power (22 W vs 60 W).

Average cluster height was lower for the DC clusters (5,4 nm vs 6,3 nm), which could be caused by the smaller aggregation length for the DC clusters (50 mm vs 77 mm).

Sample ID	Deposition time (min)	L aggr (mm)	Ar flow (sccm)	V (V)	I (A)	P (W)
C21	5	50	18	266	0.083	22.1
C22	20	77	18	270	0.1	27.0
C24	15	100	18	272.6	0.1	27.3

Table 10 Overview of produced Ag cluster samples with DC sputtering

Sample ID	Depostion time (min)	L aggr (mm)	Ar flow (sccm)	RF forward (W)	Reflected power	C_l/C_t	Bias (V)
C10	10	40	15	60	9%	80/54	-214
C11	10	77	15	60	9%	79/55	-216
C12	20	77	15	80	13%	75/57	-238
C23	20	77	20	60	9%	78/56	-207

Table 11 Overview of Ag cluster samples produced with RF sputtering

3.7.4 Ge clusters

The produced Ge cluster samples were insufficient for further analysis. The reason for the small amount of samples was that the germanium target broke after a 270 minute deposition. Figure 51 shows a picture of the broken target.

Figure 51 Broken germanium target

3.8 Discussion

3.8.1 Analysis

Analysis of the produced samples was performed by making AFM images of the sample (size range 2x2 µm to 10x10 µm), and further analyzing these images with help of the Gwyddion software. A lot of manual actions are needed for the analysis: Placing the sample in the AFM, setting the AFM and analyzing the resulting pictures with Gwyddion. All these actions bring uncertainties into the measurements, and especially the last step requires judgment because there is no automated analytical function for determining cluster height.

Furthermore, it happened that it wasn't possible to produce sharp AFM images of a sample, without apparent reason. In this case, the sample had to be produced again, making it harder to compare with the original series.

During analysis, the part of the sample that was measured turned out to have a large influence on the number of clusters that were observed. Moving the sample by just a few µm changed the AFM image vastly on various occasions. When possible, the averages of 3 different AFM results per sample were taken to account for this.

3.8.2 Possible future improvements

For improving future performance of the cluster source, a number of possibilities can be explored.

It has been observed that adding helium as a second flow gas next to argon significantly improves clustering of particles.[60] In this mixture, He primarily responsible for the cluster condensation process and the He partial pressure can be used to control cluster size distribution: higher He partial pressure leads to smaller clusters.[60]

Using liquid nitrogen as a coolant instead of cooling water will keep the source temperature more stabile. Temperature differences may effect cluster production and thereby affect the reproducibility.[60, 61]

Increasing the Ar flow rate improves cluster production and aggregation. The flow rate was limited by the capacity of the pump that was installed (520 l/s). Installing a higher capacity pump allows using higher flow rates. Higher pressure in the cluster source creates a higher pressure ratio between the cluster source and the deposition chamber, which is the driving force for clusters deposition. Increasing the pressure in the cluster source can also be done by installing smaller apertures on the exit of the cluster source.

In the current setup, a tube was installed in the deposition chamber to prevent the cluster beam from spreading and cluster being deposited on the chamber walls. It might be possible that the tube causes turbulence in the beam, and that removing the tube gives a smoother cluster beam and more even deposition of clusters on the substrate.

Finally, the installation of a quadrupole mass filter unit will allow mass selection of the produced clusters as well as real time analysis of the beam, bypassing the need for time consuming and less reliable sample analysis with AFM.

4. Experimental

4.1 Device design

Figure 52 shows the design of the solar cells produced during this research project. Indium Tin Oxide (ITO) is a transparent conducting oxide serving as the front contact. A poly-glycidyl methacrylate (PGMA) layer is deposited around the edges of the sample. A layer of nanoclusters is then deposited. This is the absorbing layer of the solar cell and consists of silicon or germanium nanoclusters. A silver layer serves as the back contact and completes the solar cell.

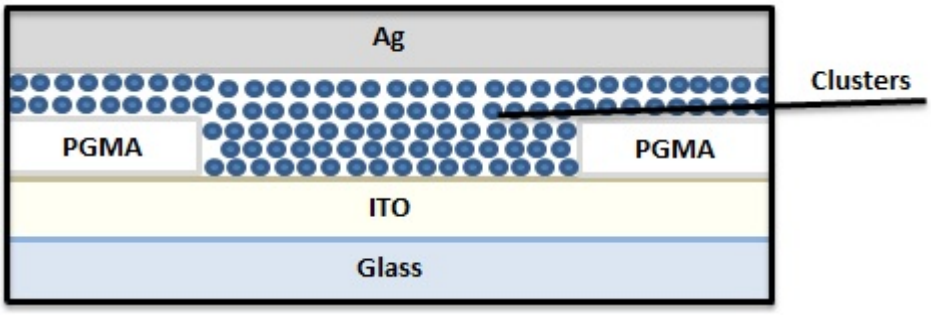

Figure 52 Schematic figure of design of Si QD Schottky solar cell

The PGMA layer is necessary because of shading effects of the sample holder: The sample holder partly covers the sample, preventing clusters to be deposited in some areas of the sample, mainly around the edges, as can be seen in Figure 53. The PGMA layer provides an extra insulating layer between the ITO and Ag layers, preventing short-circuiting in places where little or no clusters are deposited. A circular opening in the PGMA layer is the contact area between ITO and the nanoclusters.

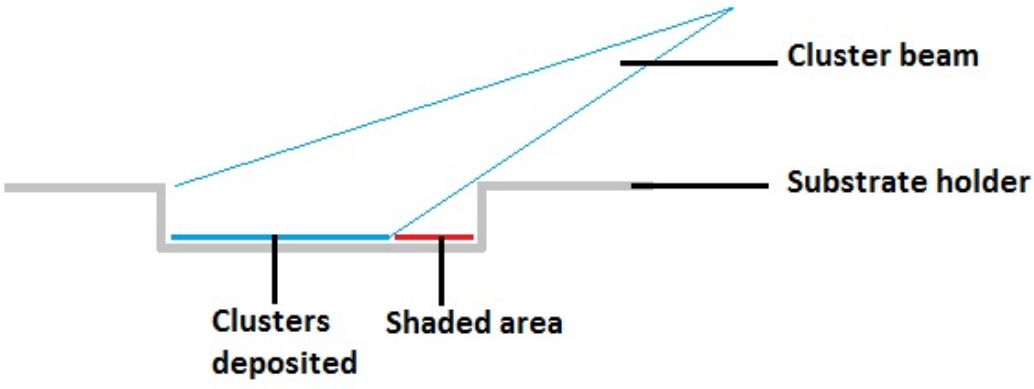

Figure 53 Shading effect caused by substrate holder

4.2 Band diagram

In this way, a schottky solar cell is formed, with charge separation taking place as described in section 2.3.1. Figure 54 gives the energy band diagram of such a cell. Varying the QD size changes the absorption and electrical characteristics of the cell. The ability to tune the bandgap gives this type of cell the flexibility to be used in various applications as described in section 2.1.

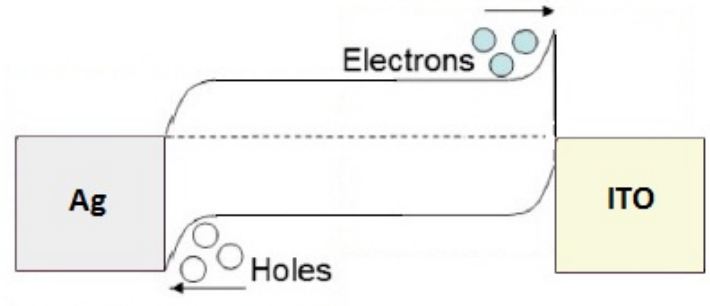

Figure 54 Band diagram of Si QD Schottky solar cell

4.3 Materials & methods

ITO

The ITO layer was deposited on a 10x10 cm glass plate using a RF magnetron sputtering system. The RF magnetron sputtering system used is a fully automated multitarget system (Kurt J Lesker Company) named SALSA (Sputtering Apparatus for Light Scattering Applications). The plasma power is supplied by a 1.6 kW RF Hüttinger power generator. After ITO deposition 1x1 cm pieces were cut using a glasscutter.

PGMA

The PGMA layer was deposited using an initiated chemical vapor deposition (iCVD) reactor called PANDA (Polymer Apparatus for New and Daring Applications). More information can be found in reference [62]. A mask was used to create the round opening in the center of the 1x1 cm substrate.

Cluster source

The nanoclusters were deposited using the clustersource setup described in section 3.

Ag

The Ag back contact was deposited using a RF sputtering system called Zeester. The plasma power is supplied by a RF power products RF5S power generator. The flow gas is Ar, and is controlled by a MKS flow controller.

DEKTAK

The PGMA surface profiles were obtained using a DektakXT (Bruker Corporation) system.

SolSim

Dark and illuminated current density versus voltage (*J-V*) measurements have been carried out using a dual beam solar simulator from WACOM, Japan, delivered by Voss Electronic in Germany. The illumination is calibrated to the AM1.5 spectrum (1000 W/m2). A computer controlled Keithley 238 Ammeter is used as voltage source and current meter, using a four point probe configuration.

4.4 Results

ITO

The ITO layer was deposited at 300 W during 940 second on a 10x10 cm glass plate, resulting in a 160 nm thick layer. The sheet resistance was measured using a 4-point probe and was 30 Ω/square in the middle and 50 Ω/square at the sides of the plate.

PGMA

Figure 55 shows the profile of a PGMA layer on ITO. The opening in the layer is clearly visible. The diameter of the opening is approximately 5 mm, and the thickness of the PGMA layer is in the order of 350 nm.

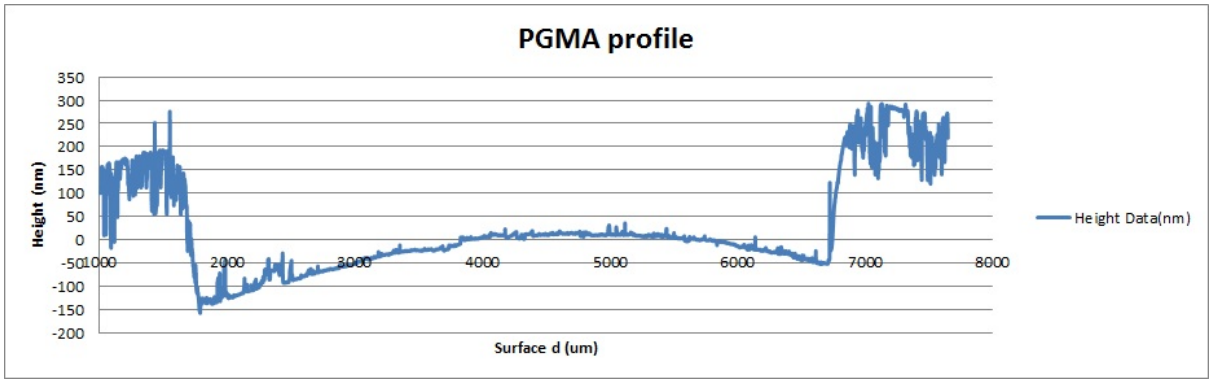

Figure 55 PGMA layer profile

Nanocluster deposition

Two cells of the abovementioned design have been produced. Table 12 shows the details of the nanoclusters deposition for both cells.

Sample	Cluster material	Aggregation length (mm)	Gas flow rate (sccm)	DC Power (W)	Deposition time (minutes)
A	Si	38	30	71.02	120
B	Ge	80	30	121.38	270

Table 12 Overview of the settings used to produce the clusters for the solar cells

Ag deposition

The silver back contact was deposited with the Zeester RF magnetron sputtering setup. A 5 minute deposition at 100 W forwarder RF power and an Ar flow of 50 sccm resulted in 175 nm thick Ag layer.

Figure 56 shows a picture of a finished cell. The mark of the substrate holder is clearly visible, as there is no silver deposited on the glass. The hole in the PGMA layer can also be seen.

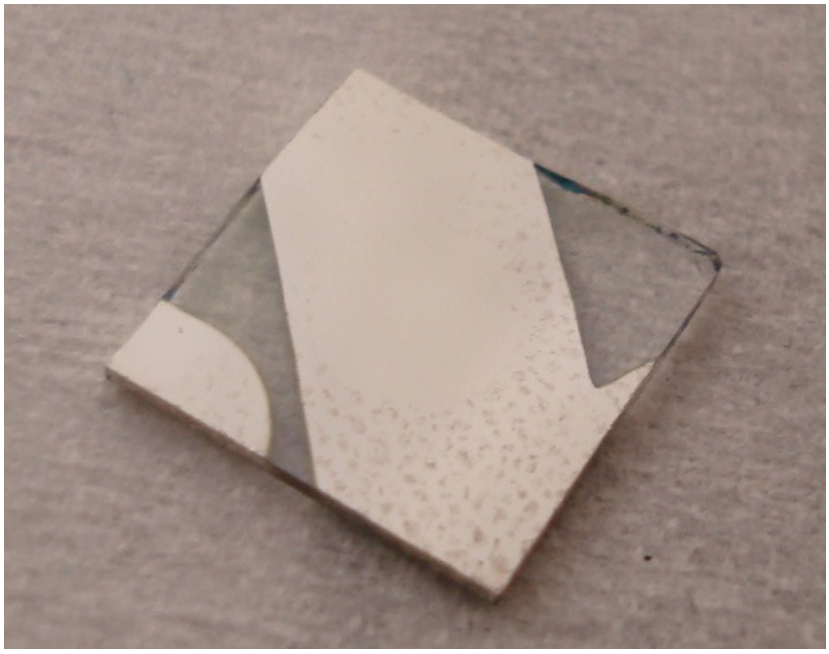

Figure 56 Finished solar cell

Solsim

Figure 57 shows the J-V characteristics of sample A for dark conditions and AM 1.5 conditions. In both cases, the curve is a straight line through the origin, indicating a short-circuited cell.

The J-V curve for sample B is similar to sample A and is therefore not shown here. Sample B was also short-circuited.

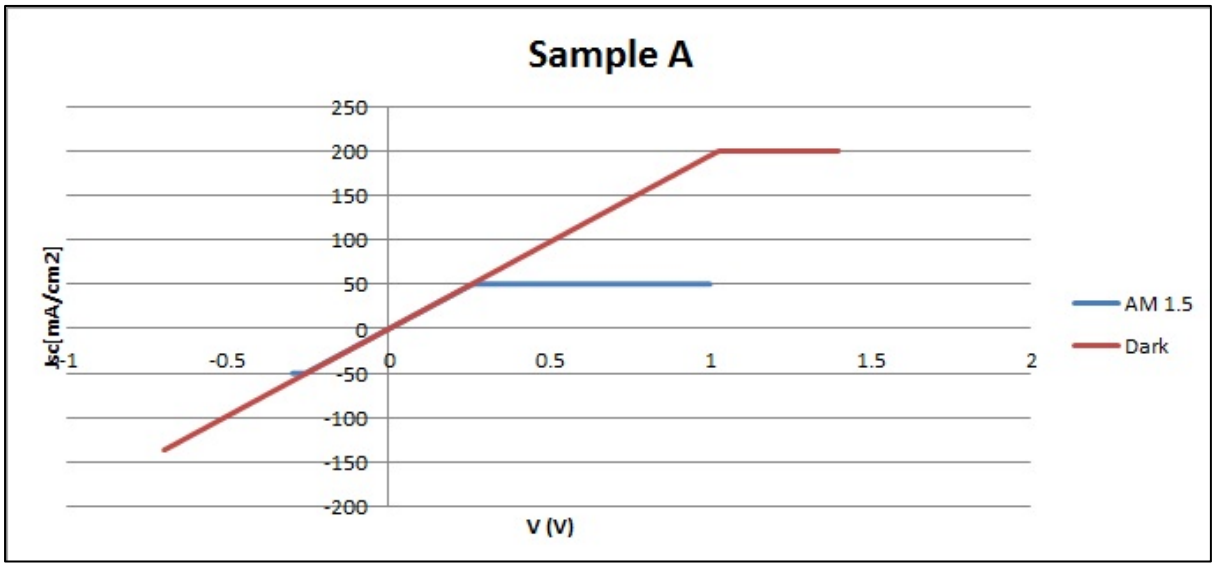

Figure 57 Solar simulation results for sample A

4.5 Discussion

The most obvious reason for the short-circuiting of both cells is that the cluster layer wasn't thick enough. Even with the long deposition times it's likely that not even a monolayer of clusters was created and the Ag layer was in direct contact with the ITO layer.

A secondary reason can be the melting of the PGMA layer. In Figure 56 spots can be seen where the PGMA layer was deposited. The heat produced by the Ag sputtering seems to have (partly) melted or broken down the PGMA layer. This layer is critical for keeping the Ag and ITO layer isolated and failure of the layer can lead to short circuiting.

For future research a couple of opportunities to improve the design should be explored. First of all, optimizing the cluster source deposition should help creating a thick enough cluster layer. Gaining more insight in the working mechanism of the cluster source and therefore improving control of the clusters that are produced is in important step. Secondly, using an isolation layer that is better resistant to the high temperatures of the RF magnetron used for sputtering the Ag layer will prevent this layer from breaking down and causing the cell to short circuit. Finally, using Al instead of Ag as a back contact might improve the solar cell's efficiency, since Al has a lower work function than Ag. The difference in work function between the back and the front (ITO) contact increases, which should lead to more band bending and better charge separation.

References

1. 2010 key world energy statistics. International Energy Agency; 2010.

2. World energy outlook 2010. International Energy Agency; 2010.

3. Borenstein S. The market value and cost of solar photovoltaic electricity production. ; 2008. Report nr CSEM WP 176.

4. Price S, Margolis R, et al. 2008 solar technologies market report. ; 2010.

5. Branker K, Pathak MJM, Pearce JM. A review of solar photovoltaic levelized cost of electricity. Renewable and Sustainable Energy Reviews 2011 12;15(9):4470-82.

6. Shockley W, Queisser HJ. Detailed balance limit of efficiency of pn junction solar cells. J App Phys 1961;32(3):510-9.

7. Conibeer G. Third-generation photovoltaics. Materials Today 2007 11;10(11):42-50.

8. Ekimov AI, Onushchenko AA. Quantum size effect in three-dimensional microscopic semiconductor crystals. JETP Lett 1981;34(6):345-9.

9. Green MA, Conibeer G. Nanostructured silicon-based tandem solar cells. University of New South Wales, Sydney, Australia; 2009. Report nr Final report.

10. Califano M, Zunger A, Franceschitti A. Direct carrier multiplication due to inverse auger scattering in CdSe quantum dots. Appl Phys Lett 2004;84(13):p2409-3p.

11. Wang Z, Qu S, Zeng X, Zhang C, Shi M, Tan F, Wang Z, Liu J, Hou Y, Teng F, et al. Synthesis of MDMO-PPV capped PbS quantum dots and their application to solar cells. Polymer 2008 10/6;49(21):4647-51.

12. Cho EC, Green MA, Conibeer G, Song D, Cho YH, Scardera G, Huang S, Park S, Hao XJ, Huang Y, et al. Silicon quantum dots in a dielectric matrix for all-silicon tandem solar cells. Adv Optoelectron 2007;2007(69578).

13. Martí A, López N, Antolín E, Cánovas E, Stanley C, Farmer C, Cuadra L, Luque A. Novel semiconductor solar cell structures: The quantum dot intermediate band solar cell. Thin Solid Films 2006 7/26;511-512(0):638-44.

14. Inoshita T, Sakaki H. Electron-phonon interaction and the so-called phonon bottleneck effect in semiconductor quantum dots. Physica B: Condensed Matter 1996 9;227(1–4):373-7.

15. Queisser HJ. Multiple carrier generation in solar cells. Solar Energy Mater Solar Cells 2010 11;94(11):1927-30.

16. Schaller RD, Klimov VI. High efficiency carrier multiplication in PbSe nanocrystals: implications for solar energy conversion. PhysRevLett 2004;92(18):186601.

17. Conibeer G, Patterson R, Huang L, Guillemoles J, Kőnig D, Shrestha S, Green MA. Modelling of hot carrier solar cell absorbers. Solar Energy Mater Solar Cells 2010 9;94(9):1516-21.

18. Zacharias M, Heitmann J, Scholz R. Size-controlled highly luminescent silicon nanocrystals: A SiO/SiO[sub 2] superlattice approach. Appl Phys Lett 2002;80(4):p661-3p.

19. Mercaldo LV, Veneri PD, Esposito E, Massera E, Usatii I, Privato C. PECVD in-situ growth of silicon quantum dots in silicon nitride from silane and nitrogen. Materials Science and Engineering: B 2009 3/15;159-160(0):77-9.

20. Mercaldo LV, Veneri PD, Esposito E, Massera E, Usatii I, Privato C. Structural and optical properties of silicon quantum dots in silicon nitride grown in situ by PECVD using different gas precursors. Materials Science and Engineering: B 2009 3/15;159-160(0):74-6.

21. Emin S, Singh SP, Han L, Satoh N, Islam A. Colloidal quantum dot solar cells. Solar Energy 2011 6;85(6):1264-82.

22. Liu Chin-Yi, Kortshagen Uwe. A silicon nanocrystal schottky junction solar cell produced from colloidal silicon nanocrystals. Nanoscale Research Letters 2010;5(8):1253.

23. Johnston KW, Pattantyus-Abraham AG, Clifford JP. Schottky-quantum dot photovoltaics for efficient infrared power conversion. Appl Phys Lett 2008;92(15):p151115-3p.

24. Hao XJ, Cho E-, Scardera G, Shen YS, Bellet-Amalric E, Bellet D, Conibeer G, Green MA. Phosphorus-doped silicon quantum dots for all-silicon quantum dot tandem solar cells. Solar Energy Mater Solar Cells 2009 9;93(9):1524-30.

25. Hao XJ, Cho E, Flynn C, Shen YS, Park SC, Conibeer G, Green MA. Synthesis and characterization of boron-doped si quantum dots for all-si quantum dot tandem solar cells. Solar Energy Mater Solar Cells 2009 2;93(2):273-9.

26. Kim J, Yun J, Han C, Cho YJ, Park J, Park YC. Multiple silicon nanowires-embedded schottky solar cell. Appl Phys Lett 2009 OCT 5;95(14):143112.

27. Mirabella S, Agosta R, Franzò G. Light absorption in silicon quantum dots embedded in silica. J Appl Phys 2009;106(10):p103505,1, 8p.

28. Rezgui B, Sibai A, Nychyporuk T, Lemiti M, Brémond G. Photoluminescence and optical absorption properties of silicon quantum dots embedded in si-rich silicon nitride matrices. J Lumin 2009 12;129(12):1744-6.

29. WANG L, ZUNGER A. Electronic-structure pseudopotential calculations of large (approximate-to-1000 atoms) si quantum dots. J Phys Chem 1994 FEB 24;98(8):2158-65.

30. So Y, Gentle A, Huang S, Conibeer G, Green MA. Size dependent optical properties of si quantum dots in si-rich nitride/Si3N4 superlattice synthesized by magnetron sputtering. J Appl Phys 2011 MAR 15;109(6):064302.

31. Jiang C, Green M. Silicon quantum dot superlattices: Modeling of energy bands, densities of states, and mobilities for silicon tandem solar cell applications. J Appl Phys 2006 JUN 1;99(11):114902.

32. Liu M, Wang Z, He Y, Jiang X. Resonant tunneling through nano-size quantum dots embedded in amorphous tissues. Microelectron Eng 2000 MAY;51-2:119-26.

33. Mocatta D, Cohen G, Schattner J, Millo O, Rabani E, Banin U. Heavily doped semiconductor nanocrystal quantum dots. Science 2011 APR 1 2011;332(6025):77-81.

34. Erwin S, Norris D, Efros A. Doped nanocrystals. Science 2008;319(5871):1776-9.

35. Hao XJ, Cho E-, Scardera G, Bellet-Amalric E, Bellet D, Shen YS, Huang S, Huang YD, Conibeer G, Green MA. Effects of phosphorus doping on structural and optical properties of silicon nanocrystals in a SiO2 matrix. Thin Solid Films 2009 8/3;517(19):5646-52.

36. Conibeer G, Green MA, Koenig D, Perez-Wurfl I, Huang S, Hao X, Di D, Shi L, Shrestha S, Puthen-Veetil B, et al. Silicon quantum dot based solar cells: Addressing the issues of doping, voltage and current transport. Prog Photovoltaics 2011 NOV;19(7):813-24.

37. Popok VN, Barke I, Campbell EEB, Meiwes-Broer K. Cluster–surface interaction: From soft landing to implantation. Surface Science Reports 2011 10;66(10):347-77.

38. Lu J, Nagase S. Structural and electronic properties of metal-encapsulated silicon clusters in a large size range. Phys Rev Lett 2003 Mar 21;90(11):115506.

39. Salivati N, Ekerdt JG. Temperature programmed desorption studies of deuterium passivated silicon nanocrystals. Surf Sci 2009 4/15;603(8):1121-5.

40. Wang J, Liu Y, Li Y. Au@Sin: Growth behavior, stability and electronic structure. Physics Letters A 2010 6/14;374(27):2736-42.

41. SWANN S. Magnetron sputtering. Physics in Technology 1988 MAR;19(2):67-75.

42. Shaik H, Raman KHT, Rao GM. Influence of si-C bond density on the properties of a-Si1-xCx thin films. Appl Surf Sci 2012 JAN 15;258(7):2989-96.

43. Kezzoula F, Hammouda A, Kechouane M, Simon P, Abaidia SEH, Keffous A, Cherfi R, Menari H, Manseri A. Aluminium-induced crystallization of amorphous silicon films deposited by DC magnetron sputtering on glasses. Appl Surf Sci 2011 SEP 15;257(23):9689-93.

44. Honer K, Kovacs G. Integration of sputtered silicon microstructures with pre-fabricated CMOS circuitry. Sens Actuator A-Phys 2001 JUL 15;91(3):386-97.

45. Ben Abdelmournen A, Cherfi R, Kechoune M, Aoucher M. Hydrogenated amorphous silicon deposited by pulsed DC magnetron sputtering. deposition temperature effect. Thin Solid Films 2008 NOV 3;517(1):369-71.

46. Plantin P, Challah F, Carriot O, Lainata F, Ancilotti M, Gadot G, Brault P. Large area silicon epitaxy using pulsed DC magnetron sputtering deposition. Microelectron Eng 2008 MAR;85(3):636-9.

47. Guruvenket S, Ghatak J, Satyam P, Rao G. Characterization of bias magnetron-sputtered silicon nitride films. Thin Solid Films 2005 MAY 1;478(1-2):256-60.

48. Golan G, Axelevitch A, Gorenstein B. Si-C multilayer quasi crystals preparation by DC magnetron sputtering. Microelectron J 2006 DEC;37(12):1538-42.

49. Cherfi R, Abdelmoumene A, Kechouane M, Rahal A, Aoucher M, Mohammed-Brahim T. Deposition temperature effects on the characteristics of a-si:H deposited by pulsed DC magnetron sputtering. Phys Status Solidi A-Appl Mat 2009 JUL;206(7):1504-9.

50. Lee C, Jan D. DC magnetron sputtering of si to form SiO2 in low-energy ion beam. Vacuum 2006 MAY 31;80(7):693-7.

51. Shi Z, Wang Y, Du C, Huang N, Wang L, Ning C. The structure, surface topography and mechanical properties of si-C-N films fabricated by RF and DC magnetron sputtering. Appl Surf Sci 2011 DEC 1;258(4):1328-36.

52. Signore MA, Sytchkova A, Dimaio D, Cappello A, Rizzo A. Deposition of silicon nitride thin films by RF magnetron sputtering: A material and growth process study. Opt Mater 2012 FEB;34(4):632-8.

53. Hurley R, Gamble H. Thin film sputtered silicon for silicon wafer bonding applications. Vacuum 2003 MAR 10;70(2-3):131-40.

54. Fukaya K, Tabata A, Mizutani T. Influence of target direct current bias voltage on the film structure of hydrogenated microcrystalline silicon prepared by direct current-radiofrequency coupled magnetron sputtering. Thin Solid Films 2005 MAY 1;478(1-2):132-6.

55. Biederman H, Stundzia V, Slavinska D, Zalman J, Pesicka J, Vanecek M, Zemek J, Fukarek W. Composite germanium/C : H films prepared by DC unbalanced magnetron sputtering. Thin Solid Films 1999 AUG 30;351(1-2):151-7.

56. Pietralunga SM, Fere M, Lanata M, Radnoczi G, Misjak F, Lamperti A, Martinelli M, Ossi PM. Sputtered ge-on-si heteroepitaxial pn junctions: Nanostructure, interface morphology and photoelectrical properties. Microelectron Eng 2011 APR;88(4):518-21.

57. Pietralunga SM, Fere M, Lanata M, Piccinin D, Radnoczi G, Misjak F, Lamperti A, Martinelli M, Ossi PM. Heteroepitaxial sputtered ge on si (100): Nanostructure and interface morphology. Epl 2009 OCT;88(2):28005.

58. Wegner K, Piseri P, Tafreshi H, Milani P. Cluster beam deposition: A tool for nanoscale science and technology. Journal of Physics.D, Applied Physics 2006;39(22):R439-59.

59. Smirnov BM. Chapter 5 processes and kinetics of cluster growth and decay. In: Clusters and small particles in gases and plasmas. Springer.

60. Pratontep S, Carroll S, Xirouchaki C, Streun M, Palmer R. Size-selected cluster beam source based on radio frequency magnetron plasma sputtering and gas condensation. Rev Sci Instrum 2005 APR;76(4):045103.

61. Majumdar A, Koepp D, Ganeva M, Datta D, Bhattacharyya S, Hippler R. Development of metal nanocluster ion source based on dc magnetron plasma sputtering at room temperature. Rev Sci Instrum 2009 SEP;80(9):095103.

62. Bakker R, Verlaan V, van der Werf CHM, Rath JK, Gleasonb KK, Schropp REI. Initiated chemical vapour deposition (iCVD) of thermally stable poly-glycidyl methacrylale. Surf Coat Technol 2007 SEP 25;201(22-23):9422-5.